Specific comments:

Page 6744, lines 2-6: Yes, the snow albedo increases linearly with snowfall intensity up to α_{max}. We precise at the end of the sentence: "while the snow albedo increases linearly with snowfall intensity [Boone and Etchevers 2001]." This aspect is not conserved in the new scheme. The fresh snow Albedo is computed with equation 17 and fresh snow characteristics (Age=0, density ~100 to 150 kg/m3 depending on equation 7, etc…).

Page 6744, line 14: Yes the nature is often more complex than the representation in physical models. Without vegetation, mathematically speaking, our sentence remains true. With vegetation, we agree that our representation of soil/vegetation/snow heat conduction is not perfect. However, while there is no explicit representation of a complex layer of vegetation/litter/soil in our model, it is better to have at least a good computation of the snow/soil heat conduction. This good computation of the snow/soil heat conduction will allow us to add more easily the vegetation/litter thermal effect. But this is another study.

Page 6744, line 21: Because it is a good compromise (physical precision versus numerical cost) to represent low snow depth like over mountains and boreal regions and deeper snowpack over Greenland and Antarctica. But the user can choose a different number of layers via the model namelist.

Page 6748, Section 3.1.3: The snow age, A_{sn} (days), for each layer, i, is simply the time in days since the snow has fallen ($\frac{\partial A_{sn}(i)}{\partial t} = \frac{1}{86400}$) and we don't think it requires an equation in the manuscript. However, we did add this sentence at the en of this section: "The snow age for each layer is the time, in days, since the snow has fallen. When a snowfall event occurs, the fresh snow characteristics including its age (0 at time of snowfall) are averaged out with the snow already present in the first layer according to their respective masses. Finally, when the layer thicknesses of the entire snowpack are recalculated with Equation 11 and 12, the snow age is redistributed accordingly. For example, the age of snow in the first layers can remain from 0 day to a week during winter but aging largely in spring, while the last layers age continuously."

Page 6749, line 8: We think that the error made by neglecting the process altogether is larger than the error due to the uncertainties in the HWSD database, at least at the global scale. Locally, it can be important.

Page 6753, line 9: Indeed, a value of 0.005 is generally used at the Col de Porte site [Vionnet et al. 2012]. We prefer to use the value used at global scale but the impact on the result is not important as shown by the following figure where the new model is represented in blue for a z0=0.005 and in red for z0=0.001 (this study) :
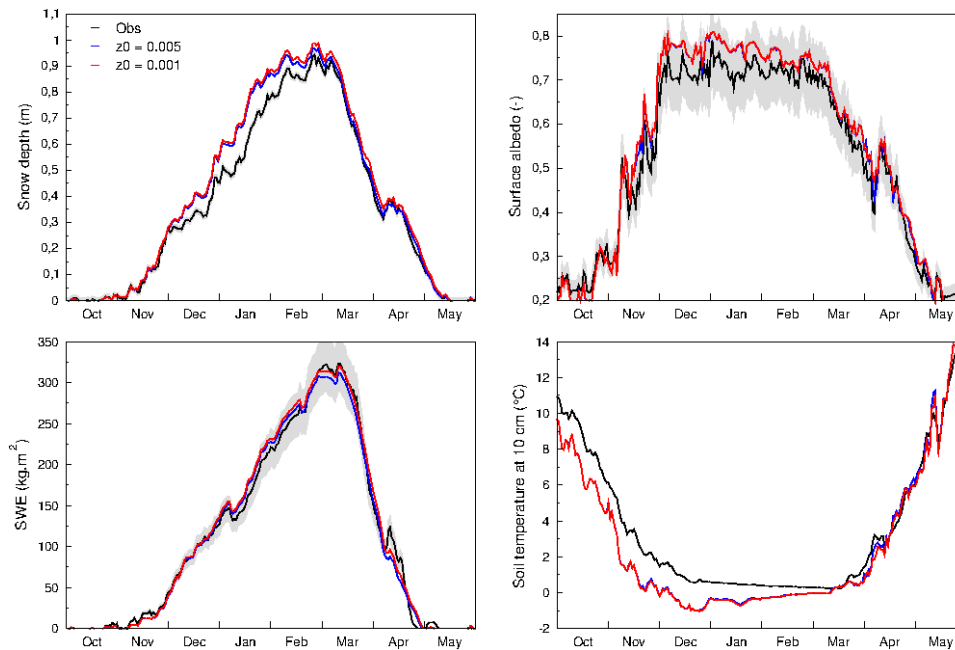
Page 6756, lines 7-10: Indeed, we do not consider blowing snow sublimation.

Page 6758, lines 3-4: We performed some local tests simulating water, ice and temperature down to 100m over a period of 300years and did not find significant differences with the simulation down to 12m. We think that it would be more important to account for the geothermal gradient than to increase the depth of the soil column. However, we agree that for very long simulations (superior to 1000years) like paleo-climatic simulations the soil should be deeper. Note that the user can prescribe its own depth and soil discretization in the namelist.

Page 6767, lines 6-7: Indeed, the default value is 5 but some tests to prepare the CNRM-CM climate model for CMIP5 experiment there is long time ago have shown that this value was too strong inducing a too low albedo during winter over forested area. So it has been reduced to 2 for global studies. We think also that this parameter should depend on vegetation type with a low value for low vegetation (~1 or 0.5) to larger value for forest (~2 or 3).

Figures 3 and 4: The most important in these two figures is the annual variability of the skill scores: bias and c-rmse . The time series in these 2 figures are mainly illustrative. As referee 2 mentions himself, it is the Figure 5 that is designed to show the differences between the model versions.

Technical corrections: All corrections have been done

Other main author's changes in manuscript :

(1) Reference added : Brown J., Hinkel K.M., & Nelson F.E. 2000. The Circumpolar Active Layer Monitoring (CALM) program: historical perspectives and initial results. Polar Geography 24(3): 165-258.
(2) Wang et al. 2015 was changed to Wang et al. 2016 (new published article: Wang, W., Rinke, A., Moore, J. C., Cui, X., Ji, D., Li, Q., Zhang, N., Wang, C., Zhang, S., Lawrence,

D. M., McGuire, A. D., Zhang, W., Delire, C., Koven, C., Saito, K., MacDougall, A., Burke, E., and Decharme, B.: Diagnostic and model dependent uncertainty of simulated Tibetan permafrost area, The Cryosphere, 10, 287-306, doi:10.5194/tc-10-287-2016, 2016)

(3) CALM data was added in Figure 12 (see responses to referee 1) and in the text.

(4) The color legend was added in Figure 13 last panel
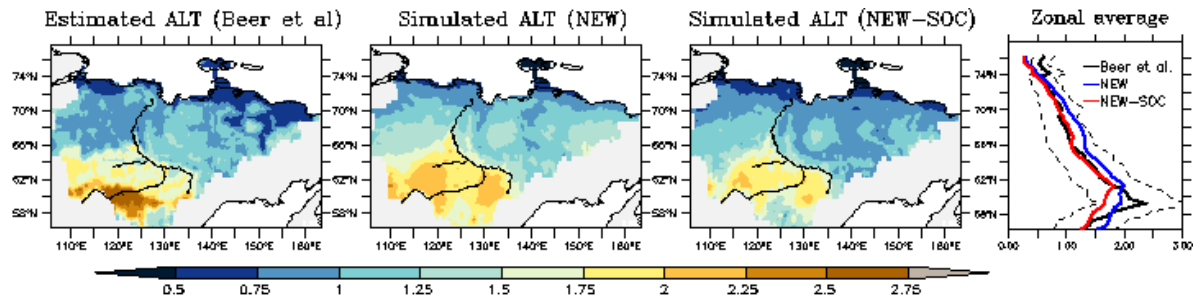
Impacts of snow and organic soils parameterization on North-Eurasian soil temperature profiles simulated by the ISBA land surface model.

B. Decharme[1], E. Brun[1,2], A. Boone[1], C. Delire[1], P. Le Moigne[1], S. Morin[3]

Corresponding Author: Bertrand Decharme (bertrand.decharme@meteo.fr)
GAME-CNRM/GMGEC/VDR
Météo-France, 42 av. Gaspard Coriolis, 31057 Toulouse, France

(1) GAME-CNRM UMR 3589, CNRS/Météo-France, Toulouse, France
(2) now at ONERC, Ministry of Ecology, Paris, France
(3) CEN ,GAME-CNRM UMR 3589, CNRS/Météo-France, Grenoble, France

1 **ABSTRACT**

2   In this study we analysed how an improved representation of snowpack processes and soil

3 properties in the multi-layer snow and soil schemes of the ISBA land surface model impacts the

4 simulation of soil temperature profiles over North-Eurasian regions. For this purpose, we refine

5 ISBA's snow layering algorithm and propose a parameterization of snow albedo and snow

6 compaction/densification adapted from the detailed Crocus snowpack model. We also include a

7 dependency on soil organic carbon content for ISBA's hydraulic and thermal soil properties. First,

8 changes in the snowpack parameterization are evaluated against snow depth, snow water

9 equivalent, surface albedo, and soil temperature at a 10cm depth observed at the Col de Porte field

10 site in the French Alps. Next, the new model version including all of the changes is used over

11 Northern-Eurasia to evaluate the model's ability to simulate the snow depth, the soil temperature

12 profile and the permafrost characteristics. The results confirm that an adequate simulation of snow

13 layering and snow compaction/densification significantly impacts the snowpack characteristics and

14 the soil temperature profile during winter, while the impact of the more accurate snow albedo

15 computation is dominant during the spring. In summer, the accounting for the effect of soil organic

16 carbon on hydraulic and thermal soil properties improves the simulation of the soil temperature

17 profile. Finally, the results confirm that this last process strongly influences the simulation of the

18 permafrost active layer thickness and its spatial distribution.

19

1. Introduction

20   Snowpack properties are known to be of primary importance for understanding the water

21 and energy budgets of the land surface, especially in mountainous and boreal regions. From

22 autumn to spring, solid precipitation is stored within the snowpack thereby modifying the

23 terrestrial albedo and roughness length, and impacting the radiative and energy fluxes at the

24 soil/atmosphere interface. During spring, the fresh water released by snowmelt contributes to soil

25 infiltration, intense streamflow and large seasonal flood events, and it directly modulates the land

26 surface evapotranspiration [Poutou et al. 2004; Niu and Yang 2006; Decharme and Douville

27 2007]. Snowpack also acts as an insulating layer at the surface which prevents significant heat loss

28 in the winter. Over North-Eurasian regions, as discussed by Paquin and Sushama [2015], this last

29 process controls the temperature of the permafrost. It is defined as a soil that remains below 0°C

30 for two or more consecutive years, and it has a significant influence on the summer permafrost

31 active layer thickness, defined as the maximum annual thaw depth. In summary, snowpack

32 properties drastically influence soil/atmosphere interactions during a large part of the year through

33 their impacts on many land surface processes.

34   Beside the importance of snowpack properties for understanding the water and energy

35 budgets of the land surface in northern regions, the physical properties of soil organic carbon (or

36 peat soil) also play a significant role. North-Eurasian soils are very rich in organic carbon because

37 the low soil temperatures in this region inhibit decomposition of dead plant material that

38 accumulates over time, thereby forming peat deposits. Soil organic carbon exhibits very different

39 hydraulic and thermal properties than mineral soil [Boelter 1969; Letts et al. 2000]. It is

40 characterized by a very high porosity, a weak hydraulic suction, and a sharp vertical hydraulic

41 conductivity profile from high values at the surface to very low values at the subsurface. This

42 generally induces a relatively wet soil with a shallow water table [Letts et al. 2000]. Its low

43 thermal conductivity and its relatively high heat capacity act as an insulator for soil temperature

44 that prevents the soil from significant warming during the summer [Bonan and Shugart 1989;

45 Lawrence and Slater 2008]. Over permafrost regions, the hydraulic and thermal properties of soil

46 organic carbon partly control the soil depth reached by the 0°C isotherm which, in turn, defines the

47 thickness of the active layer during summer [Paquin and Sushama 2015]. Through its influence on

48 soil temperature and wetness, it impacts the continental part of the carbon cycle and the land

49 surface CO_2 and CH_4 emissions to the atmosphere [Walter et al. 2006; Zimov et al. 2006].

50   In atmospheric, climate, and hydrological models, the dynamics of the snowpack and the

51 evolution of water and heat profiles within the soil are simulated using so-called Land Surface

52 Models (LSM). These LSMs, like the simple bucket scheme of Manabe [1969], were initially

53 developed over four decades ago in order to simulate realistic land surface water and energy

54 budgets in atmospheric general circulation models. Now, LSMs are used in many applications

55 such as hydrological and meteorological forecasts, global hydrological and biogeochemical

56 studies, and climate evolution prediction. Many LSMs use multi-layer soil schemes in which the

57 vertical transport of moisture and heat into the soil is explicitly solved for using diffusion

58 equations [e.g. Decharme et al. 2011]. Because the total soil depth is discretized using multiple

59 layers, these schemes allow the representation of the vertical root distribution [Zeng et al., 1998;

60 Feddes et al., 2001; Braud et al., 2005], as well as the surface/groundwater capillary exchanges

61 [e.g. Vergnes et al. 2014]. Finally, their coupling with a multi-layer snowpack scheme permits a

62 representation of the interaction between cold physical processes, such as the effect of snow on

63 soil temperature, hydrology, and freezing [Slater et al. 2001; Luo et al. 2003; Gouttevin et al.

64 2012].

65   Three major classes of snowpack schemes exist in LSMs: single-layer schemes, multi-layer

66 schemes of intermediate complexity, and detailed snowpack models. The first class was used

67 preferentially in the past within forecast and climate models. The snowpack was represented with

68 only one layer that evolves seasonally, which ~~ti~~is characterized as having a high albedo, a low

69 thermal conductivity, and_a low thermal capacity [Manabe 1969; Verseghy 1991; Douville et al.

70 1995]. More recently, these simple single-layer schemes have been replaced by intermediate

complexity models inspired by the pioneering work of Anderson [1979]. These schemes use a multi-layer approach with the minimum number of layers needed to simulate all of the macroscopic physical properties of the snowapck such as albedo, compaction, density, and water refreezing [Lynch-Stieglitz 1994; Loth and Graf 1998; Boone and Etchevers 2001; Brown et al. 2006; Oleson et al. 2010; Dutra et al. 2010; Shrestha et al. 2010; Best et al. 2011; Kuipers Munneke et al. 2011]. Finally, more complex snowpack models have been developed primarily in support of avalanche forecasting, and more generally for all applications (including process studies) requiring a detailed representation of the vertical profile of the physical properties of snow. In addition to simulating macroscopic snowpack physical properties, they explicitly account for the time evolution of the snow microstructure driven by snow metamorphism, and the multiple feedback loops involving internal snow processes and the energy and mass balance at the air/snow and snow/ground interface [Brun et al. 1989, 1992; Jordan 1991; Bartelt and Lehning 2002]. In addition, these models can serve as a reference for the development and evaluation of intermediate complexity snowpack schemes.

The Interaction-Soil-Biosphere-Atmosphere (ISBA) LSM developed at Météo-France currently uses a multi-layer approach for the snowpack [Boone and Etchevers 2001] and the soil [Boone et al., 2000; Decharme et al. 2011]. ISBA is the land surface model embedded in the SURFEX (SURFace EXternalized) modeling platform [Masson et al. 2013], which is used in all of the atmospheric meso-scale, regional-scale and global-scale models of Météo-France, as well as in regional hydrological forecasting systems, global hydrological models and model chains in support of avalanche hazard warning [e.g. Lafaysse et al., 2013; Vernay et al., in press]. The ISBA multi-layer version was evaluated over many local or regional field datasets [Boone et al., 2000; Decharme et al. 2011, 2013; Canal et al. 2014; Parrens et al. 2014; Vergnes et al. 2014; Joetzjer et al. 2015], increasing our confidence in the model's capability to simulate realistic land surface processes under a variety of climate conditions. However, over cold regions, winter top soil temperatures tend to be underestimated [Wang et al. 2016] while during summer they are

97 generally too warm. The first biases are attributable to the ISBA multi-layer snowpack scheme of

98 intermediate complexity developed by Boone et al. [2000] and based on Anderson [1979]. Indeed,

99 when the ISBA multi-layer soil scheme is coupled with the detailed Crocus snowpack model, the

100 winter soil temperature simulated at 20cm depth better matches observations over the Northern

101 Eurasian regions [Brun et al. 2013]. Secondly, ISBA only accounts for mineral soil properties

102 while many studies pointed out that the specific properties of soil organic carbon are required to

103 simulate realistic soil thermal regime over cold regions [Nicolsky et al. 2007; Beringer et al. 2001;

104 Lawrence and Slater 2008; Lawrence et al. 2008; Dankers et al. 2011].

105   The present study focuses on the impact of improving the representation of snowpack and

106 soil properties in the ISBA LSM to reproduce snow characteristics and soil temperature profiles

107 over cold regions. We replaced the original Boone and Etchevers [2001] representation of snow

108 layering, albedo and snow compaction by adapting some parameterizations used in the Crocus

109 snowpack model [e.g. Vionnet et al. 2012]. In addition, we added a parameterization of the organic

110 carbon effect on hydraulic and thermal soil properties based on the pedotransfer function of

111 Boelter [1969] and inspired by works of Letts et al. [2000] and Lawrence and Slater [2008]. The

112 changes in the snowpack parameterizations are first evaluated at the Col de Porte field site located

113 in the French Alps [Morin et al. 2012]. This dataset includes many observations at a daily time

114 step such as snow depth, snow water equivalent, surface albedo and soil temperature at 10 cm

115 from 1993 to 2011. In addition the meteorological observations required to drive the model are

116 given at a 3-hourly time step over the same period. The new parameterizations were evaluated next

117 over the North-Eurasian region using the same experimental design as Brun et al. [2013] using in-

118 situ evaluation datasets of snow depth and soil temperature profile measurements and

119 meteorological driving data from a global reanalysis. To quantify the model's ability to simulate

120 the permafrost characteristics, two additional datasets were used that estimate the location of

121 permafrost boundaries and the active layer thickness over the Yakutia region. A brief review of the

122 ISBA multi-layer model is given in section 2, all of the snowpack and soil parameterization

123 improvements and updates are presented in section 3, sections 4 and 5 describe the model

124 evaluation over the Col de Porte field site and the North-Eurasian region, respectively. Finally, a

125 discussion and the main conclusions are given in section 6.

2. Review of the ISBA land surface model

2.1.   Soil processes

128   The ISBA multi-layer model solves the one-dimensional Fourier law and the mixed-form

129 of the Richards equation explicitly to calculate the time evolution of the soil energy and water

130 budgets [Boone et al., 2000; Decharme et al. 2011]. In each layer *i*, the closed-form equations

131 between the soil liquid water content, *w* (m^3.m^{-3}), and the soil hydrodynamic parameters, such as

132 the soil matric potential, ψ (m), and the hydraulic conductivity, *k* (m.s^{-1}), are determined according

133 to the Brooks and Corey [1966] model adapted by Campbell [1974] as follows:

$$134 \quad \psi(i)=\psi_{sat}(i)\left(\frac{w(i)}{w_{sat}(i)}\right)^{-b(i)} \quad \text{and} \quad k(i)=k_{sat}(i)\left(\frac{\psi(i)}{\psi_{sat}(i)}\right)^{-\frac{2b(i)+3}{b(i)}} \tag{1}$$

135 where, *b* represents the dimensionless shape parameter of the soil-water retention curve, w_{sat}

136 (m^3.m^{-3}) the soil porosity, and ψ_{sat} (m) and k_{sat} (m.s^{-1}) the soil matric potential and hydraulic

137 conductivity at saturation, respectively. In this study, the heat and soil moisture transfers within the

138 soil are computed using 14 layers up to a 12 m depth. The depth of the 14 layers (0.01m, 0.04m,

139 0.1m, 0.2m, 0.4m, 0.6m, 0.8m, 1.0m, 1.5m, 2.0m, 3.0m, 5.0m, 8.0m, 12.0m) have been chosen to

140 minimize numerical errors in solving the finite-differenced diffusive equations, especially in the

141 uppermost meter of the soil [Decharme et al. 2011]. Saturated hydraulic conductivity, matric

142 potential at saturation, and porosity of the mineral soil are related to the soil texture [Noilhan and

143 Lacarrère 1995]. The total heat capacity of the mineral soil in each layer is computed as the sum of

144 the soil matrix, water and ice heat capacities weighted by the volumetric water and ice content

145 [Peters-Lidard et al. 1998]. The thermal conductivity of the mineral soil is computed via a more

7

146 complex combination of water, ice and soil conductivities as proposed by Peters-Lidard et al.

147 [1998].

148 The soil ice content tendency (partial time derivative) is solved explicitly in each layer of

149 the soil and accounts for ice sublimation and vegetation insulation effect at the surface [e.g. Boone

150 et al., 2000]. The liquid water content that can freeze is limited by a maximum value, w_{lmax} (m³.m⁻

151 ³), computed as a function of temperature based on the Gibbs free-energy method [Fuchs et al.

152 1978]:

153 $$w_{l\max}(i) = w_{sat}(i) \times \min\left[1.0, \left(\frac{L_f}{g\,\psi_{sat}(i)} \frac{T_g(i) - T_f}{T_g(i)}\right)^{-1/b(i)}\right]$$ (2)

154 where w_{sat} (m³.m⁻³) is the soil porosity in each layer i, T_g (K) the soil temperature, g (m.s⁻²) the

155 terrestrial gravity constant, T_f (273.16 K) is the triple-point temperature for water, and L_f (3.337

156 $\times 10^5$ J.kg⁻¹) the latent heat of fusion. The total water content in each soil layer is conserved during

157 phase changes. When the soil freezes, the liquid water content will decrease owing to a

158 corresponding increase in soil ice content. Finally, the maximum temperature, T_{max} (K), used for

159 phase changes can be determined via the same Gibbs free-energy method :

160 $$T_{\max}(i) = \frac{L_f T_f}{L_f - g\,\psi(i)}$$ (3)

161 where the soil matric potential ψ is defined using Equation 1. Thus, this scheme induces

162 dependencies of water phase changes to soil textures and to the degree of soil humidity. The

163 coarser the soil texture, the larger the quantity of water that will freeze at a given temperature. As

164 the soil becomes dry, the temperature that allows freezing drops. More details can be found in the

165 supplementary   material   of   Masson   et   al.   [2013]   (http://www.geosci-model-

166 dev.net/6/929/2013/gmd-6-929-2013-supplement.pdf)

167 *2.2.   Snowpack internal processes*

168 The original ISBA explicit multi-layer snow scheme developed by Boone and Etchevers

169 [2001] is a snowpack scheme of intermediate complexity made in order to take into account for

170 some processes such as snow mass and heat vertical redistribution, snow compaction, water

171 percolation and refreezing, and explicit heat conduction at the snow/soil interface. Many of theses

172 processes, such as snow compaction or absorption of solar energy, are based on works of

173 Anderson [1976] and Loth et al. [1993]. The thermal conductivity of snow (Appendix A) is

174 computed via the snow density [Yen 1981]. An additional term depends on the snow temperature

175 to account for vapor transfer through the snowpack [Sun et al. 1999]. The time evolution of the

176 snow mass is linked to snowmelt, water freezing, evaporation, and liquid flow. The liquid water

177 content into the snowpack is simulated as a succession of bucket-type reservoirs. A maximum

178 liquid water holding capacity (W_{lmax}) is computed in each layer. It varies from 3% to 10% of the

179 snow mass according to a decrease in snow density after Anderson [1976]. A liquid water flux is

180 generated when the liquid water content exceeds this threshold. More details can be found in

181 Boone and Etchevers [2001] and only internal physical processes of the snowpack discussed in

182 this study are described below.

183   *2.2.1. Snow layering*

184   In the original ISBA explicit snow scheme, three-layers are used for snow layering because

185 it is considered to be the minimum number required to resolve adequately the snow thermal profile

186 within the snowpack [Lynch-Stieglitz 1994; Loth and Graf, 1998; Boone and Etchevers 2001]. The

187 algorithm that computes the snow grid thicknesses Δz of each layer, i, is described as follows:

188
$$\begin{vmatrix} \Delta z(1) = \delta 0.25 h_{sn} + (1-\delta)0.05 \\ \Delta z(2) = \delta 0.5 h_{sn} + (1-\delta) \times \min[0.5, 0.05 + 0.34(h_{sn} - \Delta z(1))] \\ \Delta z(3) = \delta 0.25 h_{sn} + (1-\delta)(h_{sn} - \Delta z(1) - \Delta z(2)) \end{vmatrix} \text{ with } \begin{vmatrix} \delta = 1 & \forall (h_{sn} \leq 0.2) \\ \delta = 0 & \forall (h_{sn} > 0.2) \end{vmatrix} \quad (4)$$

189 where h_{sn} (m) is the total snow depth. As long as the snow remains below 0.2m, the fraction of the

190 total depth that defines the thickness of each layer remains with a fine resolution at the top and the

191 base of the snowpack. When the snow depth exceeds 0.2m, the thickness of the first layer remains

192 equal to 0.05m, in order to adequately solve the diurnal cycle of the surface energy balance. In

193 addition, for large snow depth values, the second layer thickness cannot exceed 0.5m because

194 density and heat vertical gradients are generally the largest near the top of the snowpack. The

9

195 vertical grid is updated at the beginning of each time step before the computation of the other

196 snowpack internal processes.

2.2.2. Snow compaction

198 The evolution of snow density, ρ_{sn} (kg.m^{-3}) in each layer, i, is the sum of snow compaction

199 due to change in snow viscosity, η (~~Pa.s~~Pa s), and settling due to freshly fallen snow, ξ (s^{-1}),

200 following Anderson [1976] and Loth et al. [1993]:

$$201 \quad \frac{1}{\rho_{sn}(i)}\frac{\partial \rho_{sn}(i)}{\partial t} = \frac{\sigma(i)}{\eta(i)} + \xi(i) \quad \text{with} \quad \sigma(i) = g\sum_{j=1}^{i}[\Delta z(j)\rho_{sn}(j)] \tag{5}$$

202 where σ (Pa) is the snow vertical stress. The snow viscosity and settling of new snow are solved

203 using two empirical exponential functions of snow density and temperature, T_{sn} (K), :

$$204 \quad \begin{vmatrix} \eta(i) = v_0\exp(v_1(T_f - T_{sn}(i)) + v_2\rho_{sn}(i)) \\ \xi(i) = s_0\exp(-s_1(T_f - T_{sn}(i)) - s_2 \times \max(0, \rho_{sn}(i) - \rho_d)) \end{vmatrix} \tag{6}$$

205 where $v_0 = 3.7\ 10^7$ ~~Pa.s~~Pa s, $v_1 = 0.081$ K^{-1}, $v_2 = 0.018$ m^3.kg^{-1}, $s_0 = 2.8\ 10^{-6}$ s^{-1}, $s_1 = 0.04$ K^{-1}, $s_2 =$

206 0.046 m^3.kg^{-1}, and $\rho_d = 150$ kg.m^{-3} are empirical parameters calibrated by Anderson [1976]. The

207 minimum density of snow is constrained to be 50kg.m^{-3}. The snowfall density, ρ_{snew} (kg.m^{-3}), is

208 expressed as a function of wind speed, V_a (m.s^{-1}), and air temperature, T_a (K), following an

209 experimental study of Pahaut [1976] :

$$210 \quad \rho_{snew} = a_\rho + b_\rho(T_a - T_f) + c_\rho V_a^{1/2} \tag{7}$$

211 where the coefficients $a_\rho = 109$kg.m^{-3}, $b_\rho = 6$ kg.m^{-3}.K^{-1}, and $c_\rho = 26$ kg.s$^{1/2}$.m$^{-7/2}$.

2.2.3. Transmission of solar radiation and Snow albedo

213 The absorption of incident shortwave solar radiation, R_{SW} (W.m^{-2}), within the snowpack is

214 solved over a single spectral band. It uses an exponential decrease of incoming radiation with

215 snow depth [Anderson 1976; Loth et al. 1993]. So, the net shortwave radiation Q_{sn} (W.m^{-2})

216 absorbed by the snow level, i, is given by:

$$217 \quad Q_{sn}(i) = (1 - \alpha_{sn})R_{sw}\exp\left(-\sum_{j=1}^{i}[\beta_{sn}(j)\Delta z(j)]\right) \tag{8}$$

218   where α_{sn} is the dimensionless snow albedo, and β_{sn} (m^{-1}) the extinction coefficient of snow which

219   is given by :

220    $$\beta_{sn}(i) = C_v \, \rho_{sn}(i) / \sqrt{d_{opt}(i)} \qquad\qquad (9)$$

221   As shown by Bohren and Barkstrom [1974], this extinction of snow is directly related to its

222   density, the optical diameter d_{opt} (m), and a constant $C_v = 3.8 \, 10^{-3} \mathrm{m}^{5/2}.\mathrm{kg}^{-1}$. The optical diameter is

223   empirically linked to the snow density following a simple polynomial regression established by

224   Anderson [1976]:

225    $$d_{opt}(i) = \min\left(d_{max}, g_1 + g_2 \times \rho_{sn}(i)^4\right) \qquad\qquad (10)$$

226   where d_{max} (m) is the maximum value equal to $2.796 \, 10^{-3}$m, and the coefficients $g_1 = 1.6 \, 10^{-4}$m,

227   and $g_2 = 1.1 \, 10^{-13} \mathrm{m}^{13}.\mathrm{kg}^{-4}$ were calibrated by Anderson [1976]. The time evolution of snow albedo

228   is modelled in a simple way using time constants after Douville et al. [1995]. A linear decrease

229   rate is used for dry snow and an exponential decrease is used for wet snow while the snow albedo

230   increases linearly with snowfall intensity [Boone and Etchevers 2001]. The snow albedo is

231   constrained to be between its minimum value, $\alpha_{min} = 0.5$, and its maximum, $\alpha_{max} = 0.85$.

232   **3. Changes in explicit snow and soil schemes**

233   *3.1.   Changes in snowpack internal processes*

234   *3.1.1. Snow layering*

235   Detailed snowpack models use more than a dozen layers to simulate well the snow thermal

236   profile and the snowpack stratigraphy [Armstrong and Brun 2008; Vionnet et al 2012]. This

237   configuration allows a good computation of the diurnal cycle through the use of fine top layers,

238   while bottom layers are also sufficiently thin to ensure a good computation of the heat conduction

239   at the snow/soil interface. However, these models were rarely used in global atmospheric, climate,

240   and/or hydrological models due to their high computational costs partly due to the use of a large

241   number of layers. For this reason, the multi-layer snow scheme in ISBA was developed using only

242   three layers representing a good compromise between a reasonable simulation of the snow thermal

243 profile [Boone and Etchevers 2001] and a low computing time. Today, such computational

244 limitations are less of a constraint and a larger number of layers can be used in this scheme. The

245 number of snow layers in ISBA was increased to 12 with two fine layers at the top and the bottom

246 of the snowpack using the following simple algorithm:

$$\left| \begin{array}{l} \Delta z(i) = \min\left(\delta_i, \dfrac{h_{sn}}{12} \right) \quad \forall i \leq 5 \quad \text{or} \quad \forall i \geq 9 \\[2mm] \Delta z(6) = 0.3 d_r - \min[0, 0.3 d_r - \Delta z(5)] \\[1mm] \Delta z(7) = 0.4 d_r + \min[0, 0.3 d_r - \Delta z(5)] + \min[0, 0.3 d_r - \Delta z(9)] \\[1mm] \Delta z(8) = 0.3 d_r - \min[0, 0.3 d_r - \Delta z(9)] \\[2mm] d_r = h_{sn} - \displaystyle\sum_{i=1}^{5} \Delta z(i) - \sum_{i=9}^{12} \Delta z(i) \end{array} \right. \tag{11}$$

247   (11)

248 where the constants are defined as: $\delta_1 = 0.01$m, $\delta_2 = 0.05$m, $\delta_3 = 0.15$m, $\delta_4 = 0.5$m, $\delta_5 = 1$m, $\delta_9 =$

249 1m, $\delta_{10} = 0.5$m, $\delta_{11} = 0.1$m, and $\delta_{12} = 0.02$m. For a snow depth below 0.1m, each layer has the

250 same thickness of 0.00833m. When the snow depth is above 0.2m, the thicknesses of the first and

251 the last layers reach their constant values of 0.01m and 0.02m respectively to reasonably resolve

252 the diurnal cycle and the snow/soil heat exchanges. However, to keep as much as possible the

253 information of an historical snowfall event, the grid thicknesses are updated only if the two first

254 layers or the last layer become too small or too large. This condition can be summed-up as

255 follows:

256     $\Delta z(i) < \dfrac{1}{2}\min\left(\delta_i, \dfrac{h_{sn}}{12} \right) \quad \text{or} \quad \Delta z(i) > \dfrac{3}{2}\min\left(\delta_i, \dfrac{h_{sn}}{12} \right) \quad \forall i = \{1,2,12\}$ (12)

257 For example, for a total snow depth of 1m, if the thickness of the top layer becomes lower than

258 0.005m or greater than 0.015m at the beginning of a time step, the layer thicknesses of the entire

259 snowpack are recalculated with Equation 9 11 and the snow mass and heat are redistributed

260 accordingly. A similar algorithm was also developed for the 6 and 9 layer cases, but these results

261 are not reported here. In terms of snowpack layering, the main difference with the Crocus scheme

262 is the fact that the total number of layers is constant, while in Crocus only the maximum number of

263 layers is specified (typically 20 or 50) and the model dynamically uses a number of layers which

264 varies in time within this pre-defined constraint [Vionnet et al 2012].

265   *3.1.2. Snow compaction ~~and snowdrift events~~*

266   In the new version of the snow scheme, the evolution of snow density in each layer is due

267 to snow compaction resulting from changes in snow viscosity [Brun et al 1989] and <u>wind-induced</u>

268 <u>densification of near surface snow layers</u> ~~snow densification of surface layers during snowdrift~~

269 ~~events~~ [Brun et al. 1997]. <u>This wind-driven compaction process</u> ~~Snowdrift~~ is assumed to occur

270 when wind velocity exceeds a threshold value that depends on snow surface characteristics. This

271 process is especially important for simulating the evolution of the snow density over polar regions.

272 Brun et al. [1997] pointed out that this process is also critical for reproducing the snow thermal

273 conductivity and the snow temperature profile over these regions. Therefore, the time tendency of

274 snow density in each layer is computed as follows:

275 $$\frac{\partial \rho_{sn}(i)}{\partial t} = \rho_{sn}(i)\frac{\sigma(i)}{\eta(i)} + \max\left(0, \frac{\rho_{wmax} - \rho_{sn}(i)}{\tau_w(i)}\right) \qquad (13)$$

276 where ~~ρ_{drift}~~ ρ_{wmax} (kg.m^{-3}) is the maximum density equal to 350 kg.m^{-3} below which the snow

277 densification occurs during <u>wind-driven compaction</u>~~snowdrift events~~, ~~τ_{drift}~~ τ_w (s) the compaction

278 rate of this process (Appendix B), and σ (Pa) the vertical stress in each layer. This stress is

279 computed as the weight of the overlaying layers. At the top of the snow pack, half the mass of the

280 uppermost layer is used. The vertical stress in each layer is then given by:

281 $$\left| \begin{array}{l} \sigma(1) = \frac{g\Delta z(1)\rho_{sn}(1)}{2} \\ \sigma(i) = g\sum_{j=1}^{i-1}\left[\Delta z(j)\rho_{sn}(j)\right] \quad \forall i > 1 \end{array} \right. \qquad (14)$$

282   The snow viscosity is a function of snow density, temperature, and liquid water content, W_l

283 (kg.m^{-2}), and it is given as follows:

$$284 \quad \left| \begin{array}{l} \eta(i) = \dfrac{\eta_0}{f_W(i)} \dfrac{\rho_{sn}(i)}{\rho_0} \exp\big(a_\eta \times \min\big(\Delta T_\eta, T_f - T_{sn}(i)\big) + b_\eta \rho_{sn}(i)\big) \\[2mm] f_W(i) = 1 + 10 \times \min\left(1.0, \dfrac{W_l(i)}{W_{l\max}(i)}\right) \end{array} \right. \qquad (15)$$

285   where η_0 (~~Pa.s~~Pa s) is a reference viscosity equal to 7622370 ~~Pa.s~~Pa s, ρ_0 (kg.m^{-3}) is a reference

286   density equal to 250kg.m^{-3}, W_{lmax} (kg.m^{-2}) represents the maximum liquid water holding capacity

287   (e.g. section 2.2) and the constants $a_\eta = 0.1$K^{-1}, $b_\eta = 0.023$ m^3.kg^{-1}, and $\Delta T_\eta = 5$K. The viscosity

288   dependence on snow temperature is limited according to Schleef et al. [2014] who pointed out that

289   the impact of snow temperature on snow densification becomes negligible at low temperatures.

290   The last dimensionless function, f_W, describes the decrease of viscosity in presence of liquid water.

291   Finally, the snowfall density is computed as previously (Equation 7).

292   *3.1.3. Transmission of solar radiation and Snow albedo*

293   The absorption of incident shortwave solar radiation, R_{SW} (W.m^{-2}), within the pack is now

294   solved over three spectral bands according to Brun et al. [1992]. The first band ([0.3-0.8] µm)

295   represents the ultra-violet and visible range, while the two others ([0.8-1.5] µm and [1.5-2.8] µm)

296   represent two near-infrared ranges. The total net shortwave radiation, Q_{sn}, absorbed by the snow

297   level i, is the sum of the absorption in each spectral bands, k, and is given by:

$$298 \quad Q_s(i) = R_{sw} \sum_{k=1}^{3}\left[\omega(k)\big(1 - \alpha_{sn}(k)\big)\exp\left(-\sum_{j=1}^{i}\big[\beta_{sn}(k,j)\Delta z(j)\big]\right)\right] \qquad (16)$$

299   where ω is the empirical weight of each spectral bands equal to 0.71, 0.21, and 0.08 for [0.3-0.8],

300   [0.8-1.5] and [1.5-2.8] µm, respectively. As previously, the extinction coefficient of snow, β_{sn},

301   depends on density and optical diameter of snow. The snow albedo, α_{sn}, is a function of the snow

302   optical diameter and of the age of the first layer of the snowpack. The age dependency is limited to

303   the first band (visible range) and aims to represent the decrease of the snow albedo by impurities

304   from deposition in a very simple way. Indeed, trace amount of light-absorbing impurities can

305   significantly reduce snow albedo in the visible range but have no effect on the near-infrared range

306 [Warren 1984]. In each band, both the albedo and the extinction coefficient of snow are computed

307 according to Brun et al. [1992] as follows:

308
$$\left|\begin{array}{l} \alpha_{sn}(1) = \max\left[0.6, \min\left(0.92, 0.96 - 1.58\sqrt{d_{opt}(1)}\right) - \min\left(1, \max\left(\frac{1}{2}, \frac{P_a}{P_{ref}}\right)\right) \times 0.2\frac{A_{sn}(1)}{A_{ref}}\right] \\ \beta_{sn}(1,i) = \max\left[40, 0.00192\,\rho_s(i)\big/\sqrt{d_{opt}(i)}\right] \\ \alpha_{sn}(2) = \max\left[0.3, 0.9 - 15.4\sqrt{d_{opt}(1)}\right] \\ \beta_{sn}(2,i) = \max\left[100, 0.01098\,\rho_s(i)\big/\sqrt{d_{opt}(i)}\right] \\ \alpha_{sn}(3) = 0.88 + 346.2d' - 32.31\sqrt{d'} \quad \text{with} \quad d' = \min\left[0.0023, d_{opt}(i)\right] \\ \beta_{sn}(3,i) = +\infty \end{array}\right.$$
(17)

309 where A_{sn} is the age of the first snow layer expressed in days, A_{ref} a reference age set to 60 days

310 that modulates the snow albedo decrease due to impurities, P_a (Pa) is the near surface atmospheric

311 pressure, and P_{ref} (Pa) a reference pressure equal to 870hPa. The optical diameter of snow is

312 simply given by Equation (10) but is now also dependent on snow age:

313 $\quad d_{opt}(i) = \min\left[d_{max}, g_1 + g_2 \times \rho_{sn}(i)^4 + g_3 \times \min(15, A_{sn}(i))\right]$
(18)

314 where g_3 is the rate of increase of the optical diameter of snow with snow age. It is set to $0.5\ 10^{-4}$

315 m.day^{-1} through calibration. The motivation to add this snow age dependency on snow optical

316 diameter is discussed in section 6.

317   The snow age for each layer is the time, in days, since the snow has fallen. When a

318 snowfall event occurs, the fresh snow characteristics including its age (0 at time of snowfall) are

319 averaged out with the snow already present in the first layer according to their respective masses.

320 Finally, when the layer thicknesses of the entire snowpack are recalculated with Equation 11 and

321 12, the snow age is redistributed accordingly. For example, the age of snow in the first layers can

322 remain from 0 day to a week during winter but aging largely in spring, while the last layers age

323 continuously.

324 *3.2.   Effects of soil organic carbon on soil hydraulic and thermal properties*

325 North-Eurasian soils are rich in organic carbon as shown in Figure 1. This figure represents

326 the soil organic carbon content of two soil horizons (0-30cm and 30-70cm) aggregated at a 0.5° by

327   0.5° horizontal resolution and estimated from the Harmonized World Soil Database (HWSD;

328   http://webarchive.iiasa.ac.at/Research/LUC/External-World-soil-database/HTML/) at a 1 km

329   resolution from the Food and Agricultural Organization [FAO 2012]. The parameterization of the

330   impact of soil organic carbon on hydraulic and thermal properties in ISBA is based on

331   pedotransfer functions of Boelter [1969], and on the work by Letts et al. [2000] and Lawrence and

332   Slater [2008]. The pedotransfer functions of Boelter [1969] link the soil water retention at different

333   pressure levels to the fiber content of a peat soil. Letts et al. [2000] describe the vertical profile of

334   hydraulic properties such as soil matric potential and hydraulic conductivity at saturation for a

335   typical organic soil. The hydraulic properties change sharply from the near surface where peat is

336   weakly decomposed (fibric soil) to the sub-surface with moderately and well decomposed peat

337   (hemic and sapric soils respectively). Lawrence and Slater [2008] proposed a linear combination

338   of such soil organic properties with the standard mineral soil properties.

339   In ISBA, before averaging soil organic with mineral properties, a typical peat soil profile is

340   computed for the model soil grid using a power function for each hydraulic property, α_{peat}, found

341   in Table 1. For each soil layer i, this function is described as:

342    $$\alpha_{peat}(i) = \alpha_{fibric} z(i)^{\beta} \quad \text{with} \quad \beta = \frac{\ln(\alpha_{sapric}/\alpha_{fibric})}{\ln(d_{sapric}/d_{fibric})} \tag{19}$$

343   where z (m) is the depth of the considered soil grid node, α_{fibric} and α_{sapric} the fibric and sapric

344   parameter values (Table 1), d_{fibric} (m) the depth arbitrarily set to 0.01m where the profile starts to

345   depart from fibric values, and d_{sapric} (m) the depth of 1m where the soil properties reach the sapric

346   values according to Letts et al. [2000].

347   To determine the organic fraction of soil, the density profile of the soil carbon must be

348   known for the entire soil grid. Using the HWSD database, the soil carbon densities in the first

349   0.3m, ρ_{top} (kg.m^{-3}), and the remaining 0.7m below, ρ_{sub} (kg.m^{-3}), are known:

350    $$\rho_{top} = \frac{S_{top}}{\Delta d_{top}} \quad \text{and} \quad \rho_{sub} = \frac{S_{sub}}{\Delta d_{sub}} \tag{20}$$

351 where S_{top} and S_{sub} (kg.m^{-2}) are the topsoil and subsoil organic carbon contents respectively, Δd_{top}

352 and Δd_{sub} (m) the thicknesses of each observed soil horizon (0.3 and 0.7m respectively). We

353 extrapolate the density present below 1m from this observed near-surface profile (Equation 20).

354 The extrapolation assumes that the carbon profile decreases sharply with soil depth according to a

355 power function. The shape of this function is given by the observed profile if the topsoil organic

356 carbon density is superior to the subsoil density. Otherwise, the density of soil carbon below a 1m

357 depth, ρ_{deep} (kg.m^{-3}), is taken equal to the subsoil density:

$$
358 \quad \left|
\begin{aligned}
&\rho_{deep} = (1-\delta)\rho_{sub} + \delta \frac{s_{top} + s_{sub}}{\Delta d_{deep} - \Delta d_{top} - \Delta d_{sub}} \left[\left(\frac{\Delta d_{deep}}{\Delta d_{top} + \Delta d_{sub}} \right)^{\beta} - 1 \right] \\
&\delta = \begin{cases} 0 & \forall \rho_{top} \leq \rho_{sub} \\ 1 & \forall \rho_{top} > \rho_{sub} \end{cases} \quad \text{and} \quad \beta = \frac{\ln\left[s_{top} / (s_{top} + s_{sub}) \right]}{\ln\left[\Delta d_{top} / (\Delta d_{top} + \Delta d_{sub}) \right]}
\end{aligned}
\right.
\tag{21}
$$

359 where Δd_{deep} (m) is an infinite soil thickness taken arbitrarily equal to 1000m.

360 Finally, the soil carbon density profile, ρ_{soc} (kg.m^{-3}), over the entire soil grid is computed

361 using these three soil horizons and a simple linear interpolation at each grid node that conserves

362 the total soil carbon mass (Figure 2). The fraction of the soil that is organic, f_{soc}, in each layer is

363 determined assuming this simple relationship:

$$
364 \quad f_{soc}(i) = \frac{\rho_{soc}(i)}{(1 - w_{sat,peat}(i))\rho_{om}}
\tag{22}
$$

365 where ρ_{om} (kg.m^{-3}) is the pure organic matter density equal to 1300 kg.m^{-3} [Farouki 1986] and

366 $w_{sat,peat}$ the porosity of the peat soil profile computed using Equation 19 and Table 1. As in

367 Lawrence and Slater [2008], this fraction is used to combine the standard mineral soil properties

368 with soil organic properties using weighted arithmetic or geometric averages, depending on the

369 parameter (Table 1). An example of this method is shown in Figure 2 for soil porosity, soil

370 saturated hydraulic conductivity and soil heat capacity.

371 4. **Local scale evaluation of snow processes at the Col de Porte site (France)**

372 *4.1.   Experimental data set*

373   The Col de Porte field site (45°17'N, 05°45'E) is located at an elevation of 1325m in the

374   French Alps near Grenoble [Morin et al. 2012]. It consists in a 50m by 50m square covered by

375   grass, mowed approximately once a month in summer depending on its growth rate. Soil textures

376   (30% clay, 60% sand) are characteristic of a sandy-clay-loam soil that is very poor in organic

377   carbon. For this reason, this site is only used to evaluate the effect of changes in snow

378   parameterizations while changes in soil physics can be not tested. The atmospheric forcing

379   variables (air temperature, rain and snow rates, air humidity, atmospheric pressure, wind speed,

380   long-wave and short-wave incident radiation) are available at a one hour time step from August 1st,

381   1993 to July 31, 2011. It consists of a combination of in-situ measurements, roughly from

382   September to June each year, and the regional reanalysis SAFRAN from June to September each

383   year (see Morin et al. [2012] for details).

384   The Col de Porte dataset includes many observations at a daily time step for evaluating

385   land surface models. In this study, the observed snow depth, surface albedo and soil temperature at

386   10 cm are used to evaluate model simulations over the entire period. The snow water equivalent

387   (SWE) is also used for this model evaluation but daily values are only available from 2001 to

388   2011. Snow depth is measured using ultra-sound depth gauges with an accuracy of 1cm. Surface

389   albedo is computed as the total daily reflected solar flux divided by the total daily incoming solar

390   flux. We estimate the uncertainty in surface albedo to be about 10% based on the 10% uncertainty

391   in observed radiative fluxes reported by Morin et al [2012]. Soil temperature is measured using

392   automatic probes with an accuracy of 0.1K. SWE is measured using a cosmic ray sensor placed on

393   the ground and exhibits an uncertainty of 10%.Three skill scores are used to compare model

394   results to the observations. The mean annual bias measures the capability of the model to

395   represents the observed mean. To evaluate the model ability to represent the observed day to day

396   variability, two statistical quantities are used; the square correlation (r^2), and the centered root

397   mean square error (c-rmse). It is computed by subtracting the simulated and observed annual

398   means from their respective time series before computing a standard root mean square error.

399 *4.2.   Model configuration*

400   Four simulations were done to evaluate the effect of the different changes in the snow

401 parameterization detailed in section 3:

402 • *CTL* uses Boone and Etchevers [2001] formulation for snow layering (3 layers), snow

403   compaction, and snow albedo as described in section 2.2

404 • *SNL* is similar to CTL in terms of snow compaction and albedo but uses the new snow

405   layering with 12 snow layers described in section 3.1.1.

406 • *CPT* uses 12 snow layers as in *SNL* but the compaction and the wind-induced densification

407   of near surface snow layers snow densification of surface layers during snowdrift events are

408   computed using formulations of Brun et al [1989 and 1997], both described in section 3.1.2.

409 • *NEW* uses all the package of snow equations described in section 3.1: 12 snow layers, the

410   new snow compaction/densification, but also the spectral representation of the snow albedo

411   (section 3.1.3).

412   For all of the simulations, the snow is assumed to cover the entire grid-cell (the snow

413 fraction set to 1) as long as the snow remains present. The effective roughness length of snow is

414 set to its usual value of 0.001m. The grid-cell is assumed to be entirely covered by grass with a

415 root depth of 1m, the leaf area index varies from 0.1 in winter to 1 in summer, and the snow-free

416 surface albedo is prescribed as 0.2. The model calculates soil temperature, moisture and ice

417 content in each of the 14 soil layers corresponding to a soil depth of 12m. The model was run with

418 a 15-minute time step from August 1st, 1993 to July 31, 2011. The model was spun-up by

419 performing fifty iterations of the first two years (August, 1993 to July, 1995). This spin-up

420 represents a total of one hundred years, and this was determined to guarantee that the water and

421 heat profiles were equilibrated over the 12m soil depth of ISBA. Results are then evaluated over

422 the entire period.

423 *4.3.   Results*

424   Figure 3 and 4 show an overview of the four simulations performed at the Col de Porte in

425   terms of snow depth, SWE, surface albedo and soil temperature at 10cm. A quick look at the time

426   series indicates that all of the model versions match the observations relatively well. However,

427   annual statistics show a clear hierarchy between the four experiments. The snow depth statistics

428   shows that the new snow compaction/densification algorithm has a positive impact on the

429   snowpack simulation. Indeed, both the *CPT* and *NEW* experiments exhibit the lowest bias and c-

430   rmse for twelve of the eighteen years. However, the comparison to SWE data does not allow a

431   discrimination between the four simulations, even if the c-rmse of the *NEW* experiment is the best

432   for seven of the ten years. The surface albedo from the *NEW* simulation is clearly better than the

433   albedo from the other experiments: bias and c-rmse are the best for all years (Figure 4). The soil

434   temperature bias and c-rmse are also reduced by the *NEW* experiment (for ten of seventeen years)

435   compared to the other simulations. Thus, accounting for different spectral bands within the snow

436   albedo calculation has a significant positive impact on the energy balance of the snow-soil system.

437   The average seasonal cycle of snow depth, SWE, surface albedo and soil temperature at

438   10cm represented in Figure 5 highlights the qualities and weaknesses of the different

439   parameterizations by focusing on the snow season (October to May). The corresponding statistics

440   for the winter (DJF), spring (MAM) and the entire period are given in Table 2. The comparison of

441   *SNL* to *CTL* indicates that the increase in number of snow layers from 3 to12 improves the snow

442   depth, SWE and winter soil temperature simulation. Change in snow compaction (from *SNL* to

443   *CPT*) improves the seasonal cycle of snow depth and SWE and especially the maximum value.

444   The seasonal and ~~global~~total biases in Table 2 verify this result and show the same behavior for

445   winter soil temperature, although it is difficult to see visually from Figure 5. For these three

446   variables, the simulated time variability is also improved from *CTL* to *SNL* to *CPT* as shown by

447   the other seasonal and ~~global~~total scores (c-rmse and r^2) in Table 2. Finally, the new spectral

448   albedo scheme (from *CPT* to *NEW*) has a drastic impact on the snowpack simulation in spring. As

449   shown by Figure 5 and Table 2, the new spectral albedos clearly improve the simulation of other

450 variables during this period. They induce a sharp springtime snowmelt with a strong decrease in

451 snow depth and SWE. The snow insulation during spring is thus less important and allows the soil

452 surface to warm up faster. As a result, the model is capable of reproducing the strong soil warming

453 observed in April (Figure 5). Not surprisingly, the soil temperature skill scores for spring and the

454 whole period are drastically improved although there is a slight degradation in winter.

455   Figure 6 shows daily mean time series of the snow density and temperature profiles

456 averaged over the snow season for each experiment. With only 3 snow layers (*CTL*), the density

457 distribution is more uniform than using the new snow layering scheme with 12 layers (*SNL*). The

458 significant densification of the bottom layers in *SNL* is the main process responsible for the snow

459 depth and SWE improvements observed in Figure 5 and Table 2. In addition, the better

460 representation of the vertical profile of density, that induces less dense and thus more insulating

461 surface snow layers from November to February, permits also to better insulate the bottom snow

462 layer from the atmosphere and results in higher bottom snow and top soil temperature. In terms of

463 snow temperature, *SNL* induces warmer bottom snow layers in winter due to the densification of

464 the lowest snow model layers and the insulation from other overlying layers. This explains the

465 skill scores improvement found in winter soil temperature in Table 2. The new snow compaction

466 scheme (*CPT*) tends to increase the density contrast between the top and the bottom snow layers.

467 The snowpack is also denser than with *SNL* leading to the strong decrease in snow depth observed

468 in Figure 5 and to the better skill scores in snow depth and SWE over each period (Table 2).

469   *CPT* also results in a small warming at the bottom of the snowpack which slightly heats the

470 soil temperature compared to *SNL*. Finally, the spectral albedo scheme (*NEW*) has a limited effect

471 on the snow density profile but results in a slightly colder snowpack than in *CPT* and even *SNL*

472 (not shown) due to the large daily winter albedos seen in Figure 5. This is the main reason for the

473 lower winter soil temperatures with *NEW* than *CPT* and *SNL* (Table 2).

474 5. **Simulations over North-Eurasia**

475 *5.1.   Numerical experiment design and observational dataset*

476   The experimental design used here is close to that proposed by Brun et al. [2013]. The

477   region considered (35°N to 85°N, 25°E to 180°E) covers Eastern-Europe, Russia and Siberia

478   (Figure 7). The ISBA land surface model is run at a 0.5° by 0.5° spatial resolution using the

479   Interim Re-Analysis (ERA-I; http://www.ecmwf.int/en/research/climate-reanalysis/era-interim)

480   [Dee et al. 2011]. ERA-I meteorological variables are extracted with a 3-hourly frequency in order

481   to represent the diurnal cycle. This reanalysis covers the time period from 1979 to the present.

482   Many details about ERA-I can be found in Dee et al [2011] and an evaluation of its performance is

483   provided in Berrisford et al. [2011]. For precipitation, the monthly ERA-I precipitation are

484   rescaled to match the observed Global Precipitation Climatology Center (GPCC) Full Data

485   Product V5 (http://gpcc.dwd.de) as proposed by Decharme and Douville [2006a]. This method

486   conserves the 3-hourly chronology of the ERA-I precipitation but ensures a reasonable monthly

487   amount [Szczypta et al. 2012]. Brun et al. [2013] pointed out the significantly better performance

488   of this ERA-I scaled GPCC forcing product in simulating North-Eurasian snowpack variables

489   compared to the ERA-I precipitation or other "state of the art" global scale atmospheric forcings.

490   To evaluate snow and soil temperature simulations, several in-situ dataset are used. As in

491   Brun   et   al.   [2013],   the   Historical   Soviet   Daily   Snow   Depth   (HSDSD;

492   http://nsidc.org/data/docs/noaa/g01092_hsdsd/index.html) compiled by Amstrong [2001] was used

493   in the current study. It consists in daily snow depth measurements taken at synoptic stations

494   following the World Meteorological Organization (WMO) standards. WMO requires the

495   measurements to be taken in bare ground open areas or clearings with regular grass cutting. These

496   snow depth data are therefore representative of open areas of bare ground or those covered with

497   very short grass. This dataset starts in 1881 with a few stations and ends in 1995. Considering that

498   ERA-I starts in 1979, the model simulations are done from 1979 to 1993 according to Brun et al.

499   [2013]. 263 HSDSD stations are available over this period with approximately half of them

500   without any missing data. We chose to use only the stations where the difference between the local

501   and the ERA-I elevation is less than 100m to avoid temperature biases for instance that would be

502   directly due to the low resolution of ERA-I. We also only kept the stations where the number of

503   days with a non zero snow depth measurement over the entire period is superior to 100 days, and

504   that have at least 8 days with snow measurement per year. With this filter, the number of available

505   stations decreases to 158, which remains acceptable. Most stations are located in Russia and

506   Western-Siberia with only a few in Eastern-Siberia (Figure 7).

507   The second source of observations is the Russian Historical Soil Temperature (RHST)

508   dataset   compiled   by   Zhang   et   al.   [2001]   over   Siberia

509   (http://data.eol.ucar.edu/codiac/dss/id=106.ARCSS078). Data coverage extends from the 1800s

510   through 1990, but is not continuous. We compared our model results over the 1979-1990 period.

511   As forSimilar to snow depth, soil temperature stations are subject to WMO standards and are

512   located in open area sites. We used the same criteria as for snow depth. Only stations with local

513   elevations close to the ERA-I altitude (less than 100m difference) are used. In addition, only

514   stations with at least 36 months of observations (at least 3 years out of 12) are kept. Most soil

515   temperature sites are collocated with snow depth sites (Figure 7). Measurements were taken at

516   20cm, 80cm, 160cm and 320cm depth. For each depth, 95, 48, 48, and 82 stations, respectively,

517   were available for model evaluation. The spatial distribution of these stations is shown in Figure 7

518   for 20cm and 160cm depths.

519   To quantify the capability of the model to simulate the permafrost characteristics, threetwo

520   datasets are used. The first dataset is the Circum-Artic Map of Permafrost and Ground Ice

521   Conditions (http://nsidc.org/data/ggd318) edited by Brown et al. [2002]. This dataset is available at

522   a 0.5° by 0.5° resolution and shows the continuous, discontinuous, isolated and sporadic

523   permafrost boundaries. The second dataset gives access to in-situ observations on active layer

524   thickness   collected   by   the   Circumpolar   Active   Layer   Monitoring   (CALM;

525   http://www.gwu.edu/~calm/) since the 1990s to 2015 [Brown et al. 2000]. Over the studied

526   domain, 233 monitoring sites are available. To compare with simulations performed at a 0.5° by

527   0.5° resolution, 89 virtual stations have been computed from the 233 original sites by averaging all

528 stations in each 0.5° by 0.5° grid-cells. The ~~second~~ last dataset is an estimate of the active layer

529 thickness over North-West-Siberia before the 1990s. This data set is based on the map of

530 landscapes   and   permafrost   conditions   in   Yakutia

531 (http://doi.pangaea.de/10.1594/PANGAEA.808240). It gives access to the mean and standard

532 deviation of the most probable active layer thickness in each grid box at 0.5° by 0.5° resolution.

533 All details can be found in Beer et al. [2013].

534 *5.2.   Model configuration*

535   Three experiments using the ISBA land surface model forced by the ERA-I scaled GPCC

536 atmospheric dataset are performed using the same configuration. In addition to the *CTL* (old snow

537 scheme) and *NEW* (new snow scheme) experiments already described in section 4, we performed

538 one simulation using the parameterization of the impact of the soil organic carbon on the

539 hydrologic and thermal soil properties. This last experiment, called *NEW-SOC,* uses the new snow

540 and soil-property schemes described in section 3.1 and 3.2, respectively. As previously, the model

541 determines the temperature, liquid water and ice content evolution in each of the 14 soil layers

542 corresponding to a total soil depth of 12m. The model is run with a 15-minute time step from

543 January 1st, 1979 to Decembre 31, ~~1993~~2013. The model's spin-up uses twenty iterations of the

544 first five years (1979 to 1983) of the atmospheric forcing, representing a total of one hundred

545 years.

546   In ISBA, we use a series of twelve sub-grid independent patches per grid cell in order to

547 account for land cover heterogeneity. Land cover parameters such as Leaf Area Index (LAI),

548 vegetation height, vegetation/soil albedos, and rooting depth are prescribed for each sub-grid

549 patch. The dominant patches present in the model over the Northern-Eurasian region are bare soil,

550 grassland/tundra, deciduous forest, coniferous boreal forest, and C3 crops in the South. The

551 fraction of each surface type within each grid box is used to compute the grid box average of the

552 water and energy budgets. Some other processes, such as surface runoff, dripping from the canopy

553 reservoir, and soil infiltration account for sub-grid parameterizations. More details can be found in

554 Decharme and Douville [2006b] and Decharme et al. [2013].

555   For all of the simulations, the grid-cell fraction covered by snow evolves according to the

556 simulated snow depth and is different for bare soil and vegetated areas (Appendix C) in each land

557 cover patch. As was the case for the Col de Porte experiment, the effective roughness length of

558 snow retains its usual value of 0.001m. The land surface parameters used by ISBA are specified

559 according to the 1-km resolution ECOCLIMAP-II database [Faroux et al., 2013]. LAI, vegetation

560 height, and vegetation/soil albedos are prescribed for the twelve vegetation sub-grid patches based

561 on a mean annual cycle at a 10-day time step. The rooting depth is specified for each vegetation

562 type according to Canadell et al. [1996]. It ranges from 0.5m to 1.5m for tundra and temperate

563 grassland, and from 2m to 3m for forest. The soil textural properties are given by the ~~HSWD~~

564 HWSD database at 1 km resolution while~~. T~~the topographic information is specified according to

565 the 30-arcsecond resolution GTOPO30 data set~~, and the topographic indexes used in the~~

566 ~~TOPMODEL runoff parameterization are given by the 1 km resolution HYDRO1K product~~

567 ~~(http://eros.usgs.gov/#/Find_Data/Products_and_Data_Available/gtopo30/hydro)~~.

568 *5.3.   Results*

569   Figure 7 presents a ~~first~~ quantitative comparison between the observed and simulated snow

570 depth and soil temperature over Northern-Eurasia. Because in-situ observations were collected in

571 bare ground open areas and/or clearings with regular grass cutting following the WMO standards

572 as mentioned previously, they are compared to snow depths and soil temperature profiles

573 simulated by the ISBA bare soil sub-grid patch alone. This patch exhibits conditions which are

574 closest to those at the corresponding field sites, as is generally the case for ISBA in this kind of

575 comparison [Decharme et al. 2013]. The simulation represented here is the *NEW-SOC* experiment

576 that seems to capture well the snow depth and soil temperature spatial distributions. For snow

577 depth, the latitudinal gradient is well respected. The lower soil temperature along a southwest-

578 northeast transect is also well simulated.

579   The seasonal cycles of daily snow depths and monthly soil temperatures (Figure 8) clearly

580   show the biases of the *CTL* simulation and the improvements due to the new snow and soil

581   representations. The seasonal cycles and the ~~global~~total skill scores are computed using the

582   measurements and simulations for all stations over the entire observed periods. ISBA globally

583   underestimates the snow depth from December through February with no clear difference between

584   *CTL* and *NEW* (or *NEW-SOC*). However, the springtime snow ~~ablation~~melting is drastically

585   improved by the new snow scheme inducing a better simulated seasonality. This fact is confirmed

586   by some other quantitative comparisons. The average number of days per year with observed snow

587   on the ground for all in-situ stations is 150.7 days. *CTL* simulates 158.7 days against 151.5 days

588   for *NEW*. On average, the last day of the snow season is day number 281.6 when starting on July

589   first. *CTL* goes beyond this date by more than 9 days while for *NEW* it is only 2 days (day number

590   283). Theses results are consistent with the model evaluation at the Col de Porte field site (section

591   4). As could be expected also, the new physical soil properties (*NEW-SOC*) play a minimal role in

592   the snow depth simulation. The seasonal cycle of the soil temperature profile confirms that the

593   new snow scheme induces a warmer soil in winter compared to *CTL,* and it strongly reduces the

594   cold bias of *CTL.* The effect of soil organic carbon is especially observable during spring and

595   summer. *NEW* exhibits a warm bias for each soil horizon while *NEW-SOC,* with more insulating

596   soils, reduces this weakness.

597   These improvement in snow depth and soil temperature are confirmed by the spatial

598   distributions of their seasonal skill scores (bias and c-rmse). Figure 9 shows the spatial

599   distributions of snow depth seasonal skill scores (bias and c-rmse) during winter and spring. No

600   clear ~~discrepancies~~ differences among these simulations appear in winter while the bias and c-rmse

601   of many stations are improved in spring by the new snow scheme. The springtime snow depth is

602   simulated in an acceptable manner by *NEW,* while *CTL* exhibits a significant overestimation. This

603   fact is confirmed by ~~global~~total scores given in each of the panels. In winter, regardless of the

604 experiments, ISBA underestimates snow depth measurements at many stations, especially in the

605 Northern and Western parts of the domains (Figure 9).

606   The spatial distribution of soil temperature seasonal skill scores simulated at 20 cm and 160

607 cm depth during winter is given in Figure 10. Regardless of the region, the generalized cold bias

608 found over all stations with *CTL* is drastically reduced with the new snow scheme and the

609 interannual variability (c-rmse) is largely improved. In summer (Figure 11), as was already shown

610 in Figure 8, *NEW-SOC* is in better agreement with observations compared to *NEW* regardless of

611 the soil horizon (lower c-rmse) even if a slight cold bias appears at the subsurface. (as shown by

612 the negative total bias found ~~Figure 11~~at 320cm depth). The *NEW* experiment overestimates the

613 temperature profile measurements at many stations near the surface, but less-so at a 320 cm depth.

614 So, it seems that the subsurface cooling in the *NEW-SOC* experiment is too intensive. But in fact at

615 320 cm depth, the simulated soil temperature in the western part of the domain remains quasi

616 unchanged between *NEW-SOC* and *NEW*. The best ~~global~~total scores ~~(or seasonal cycles in Figure~~

617 ~~9)~~ found on Figures 8 and 11 without soil organic carbon by the *NEW* experiment are in fact due to

618 error compensation between the cold and warm biases simulated in the western and eastern part of

619 the domain, respectively.

620   The effect of soil organic carbon content on soil temperature profile is also especially

621 observable in terms of the simulated permafrost characteristics. The observed and simulated

622 locations of permafrost boundaries are compared in Figure 12. Regardless of the experiment, ISBA

623 generally simulates acceptable boundaries even if the permafrost limit extends slightly too far

624 south in the western part of the domain. This figure also shows the spatial distribution of active

625 layer thicknesses simulated by the *NEW* and the *NEW-SOC* experiments. The active layer

626 thickness in the model is computed as the maximum depth reached each year by the 0°C isotherm

627 in the soil approximated via a linear interpolation between the last positive temperature node going

628 down from the surface and the first negative temperature node~~extrapolation between the last node~~

629 ~~from the surface where the soil temperature is positive and the first where it is negative~~. As

630 expected from the lower summer soil temperatures with *NEW-SOC* (Figure 9 and 11), the active

631 layer is shallower. However, this comparison with the limits of different permafrost types does not

632 allow ~~the determination of~~to determine which simulation leads to the most accurate active layer

633 thicknesses~~.~~ ~~, unless it is considered that the continuous and discontinuous permafrost exhibit~~

634 ~~generally active layers shallower than 1.5m or 2m. With this very subjective criterion~~The

635 comparison with the CALM data given in Figure 12 seems to show that *NEW-SOC* ~~seems to~~

636 simulates a more accurate spatial distribution of the active layer thickness. ~~To partially verify this~~

637 ~~hypothesis,~~This result is confirmed by Figure 13 that shows the estimated and simulated active

638 layer thicknesses over the Yakutia region. Estimations from Beer et al. [2013] present a strong

639 latitudinal gradient with an increase in active layer thickness from the north to the south. Both

640 experiments exhibit such profiles. However, the active layer thickness simulated by *NEW-SOC* is

641 in better agreement with these estimations than those by *NEW*. The latitudinal zonal average

642 confirms this result.

643 6. **Discussion and Conclusion**

644 In this study, the impact of improved representation of snowpack and soil properties in the

645 ISBA LSM to simulate snow characteristics and soil temperature profiles over cold regions was

646 analysed. ISBA's representations of snow layering, albedo, and compaction were updated by

647 incorporating some parameterizations of the detailed Crocus snowpack model. In addition, a

648 simple parameterization of the soil organic carbon effect on hydraulic and thermal soil properties

649 was introduced based on previous work [Boelter 1969; Letts et al. 2000; Lawrence and Slater

650 2008]. The model is evaluated first over the Col de Porte field site in the French Alps [Morin et al.

651 2012] in order to isolate the changes in the snowpack parameterization, and second over the North-

652 Eurasian region to analyze the model's ability to simulate snow depth, soil temperature profile and

653 permafrost characteristics.

654 Changes in the snowpack parameterizations induce noticeable improvements in the

655 simulated snow depth, SWE, surface albedo and soil temperature at the Col de Porte (field) site.

28

656   The new snow layering algorithm with 12 layers permits a refinement of the vertical distribution of

657   density and temperature in the snowpack leading to slight improvements in simulated snow depth,

658   SWE, and soil temperature during winter. The densification of the snowpack with the new

659   compaction scheme, which increases the density contrast between the top and the bottom snow

660   layers, has a significant positive impact on snow depth and winter soil temperature. Finally, the

661   new spectral albedo scheme clearly improves the simulation of the springtime surface albedo that

662   allows a better simulation of the snowpack characteristics and soil temperature during

663   ~~ablation~~melting at the end of the snow season.

664   It must be noted that the large improvement in snow albedo in spring is mainly due to the

665   use of snow age in the diagnostics of the optical diameter of snow (Equation 1~~8~~6). Without this

666   parameterization, the surface albedo is strongly overestimated in winter and, to a lesser extent in

667   spring at the Col de Porte field site, with a larger bias and c-rmse for all variables compared to the

668   new version of ISBA (not shown). The optical diameter of snow strongly controls the near-infrared

669   albedo, while impurities mostly affect the albedo in the visible spectrum [Wiscombe and Warren

670   1981]. This increase of snow optical diameter with time is necessary to represent well the decrease

671   in spectrally integrated albedo with age. However, the increase of snow optical diameter is not

672   only a function of snow density as parameterized by Anderson [1976] in Equation (~~8~~10), but it is

673   also due to snow metamorphism, which is macroscopically driven by snow temperature and snow

674   thermal gradients. Several complex parameterizations exist to explicitly represent the evolution of

675   snow optical diameter according to these processes [e.g. Carmagnola et al. 2014]. Nevertheless,

676   for the sake of simplicity, we just use a snow age dependency in the diagnostic of snow optical

677   diameter with a limitation at fifteen days (Equation 1~~8~~6). This simple diagnostic allows the model

678   to reasonably match the explicit computation of the optical diameter of snow simulated in the

679   Crocus model (not shown). The good results of the ISBA model at the Col de Porte field site

680   reinforce this choice.

681   The positive impacts of the new ISBA snow scheme are confirmed when tested over the

682   North-Eurasian region with an important number of open field in-situ snow depth and soil

683   temperature stations. Winter snow depths are slightly better simulated with the new version and

684   the winter soil temperature cold bias obtained with the old version of ISBA is clearly reduced. This

685   fact confirms that the physics used in snow schemes is of primary importance for adequately

686   simulating the snow insulating effect that prevents soil from getting too cold in winter [Slater et al.

687   2001; Luo et al. 2003; Gouttevin et al. 2012; Paquin and Sushama 2015]. Another important

688   impact of changes in the ISBA snow scheme over the North-Eurasian region is seen in spring

689   when the snowmelt is well reproduced. As shown over the Col de Porte (field) site, this is mainly

690   due to the new parameterization of spectral snow albedo.

691   Nevertheless, regardless of the model version used, simulated winter snow depths are

692   generally underestimated compared to in situ observations. The cause of this underestimation is

693   not trivial. The first source of uncertainty can be attributable to the GPCC precipitation

694   measurements that do not account for wind undercatch leading to a possible underestimation of

695   solid precipitation during winter [Adam and Lettenmaier 2003, Brun et al., 2013]. Besides

696   uncertainties related to the atmospheric forcing, the snow depth underestimation can be due to the

697   non-explicit representation of snow metamorphism. Indeed, in similar experimental conditions

698   over the Northern Eurasian region, the winter snow depth simulated by the detailed Crocus

699   snowpack model did not exhibit the same problem [Brun et al. 2013] and the main remaining

700   difference between Crocus and ISBA is now restricted almost entirely to the explicit simulation of

701   snow metamorphism. In Crocus, the viscosity of layers composed of facetted crystals and depth

702   hoar snow types is increased [Vionnet et al., 2012], which leads to reducing the overall

703   compaction rate of snowpack undergoing temperature conditions conducive to such snow types,

704   and this is consistent with the situation described above.

705   Taking into account soil organic carbon in soil physical properties logically plays a

706   minimal role in the simulated snowpack behaviour. However, this process has drastic impacts on

707 the summer soil temperature profile because it allows the soil to remain cool during spring and

708 summer as shown in previous studies [Bonan and Shugart 1989; Lawrence and Slater 2008;

709 Dankers et al. 2011]. Consequently, the spatial distribution of the permafrost active layer thickness

710 simulated by the new version of ISBA is in better agreement with estimations from Beer et al.

711 [2013] over the Yakutia region. This result is in agreement with Paquin and Sushama [2015] who

712 showed that the hydraulic and thermal properties of soil organic carbon partly control the thickness

713 of the active layer during summer. However, spatial observations of permafrost characteristics on

714 the global scale are still very scarce, and if available, they are static and don't allow the study of

715 long term trends and inter-annual variability.

716 This model validation should ideally be extended over all cold regions (e.g. North America,

717 Greenland, etc…) but considering that North-Eurasia is representative of such regions, some

718 important conclusions are confirmed by this study:

719 • An adequate simulation of snow layering and snow compaction/densification is important

720 in order to represent well winter snowpack characteristics and the soil temperature profile.

721 • Snow albedo strongly controls the simulation of the springtime snow characteristics and the

722 ~~ablation~~melting timing.

723 • To account for soil organic carbon in terms of the soil physical properties drastically

724 impacts the simulation of summer soil temperture profile and hence the permafrost active layer

725 tichkness and its spatial distribution.

726 Finally, these conclusions underscore the fact that the representation of snowpack characteristics

727 and soil thermal processes are of primary importance for studying permafrost vulnerability under

728 climate change conditions, especially if the continental carbon cycle is considered due to the

729 strong interaction between <u>soil thermal processes and</u> soil <u>organic</u> carbon ~~degradation~~

730 <u>decomposition with release of greenhouse gases.</u> ~~and soil thermal processes.~~

731

31

32

APPENDIX A

741 *Snow thermal conductivity*

742 The snow thermal conductivity is computed as a function of snow density

743 following Yen [1981]. It also accounts for vapor transfer in the snow using a simple

744 parameterization from Sun et al. [1999]. This process is especially important at low snow densities

745 and at high altitude. So the snow thermal conductivity, λ_{sn} (W.m^{-1}.K^{-1}), in each layer is given by:

746
$$\lambda_{sn}(i) = \lambda_{ice}\left(\frac{\rho_{sn}(i)}{\rho_w}\right)^{1.88} + \frac{P_0}{P_a} \times \max\left(0, k_1 - \frac{k_2}{T_{sn}(i) - k_3}\right) \tag{A1}$$

747 where λ_{ice} (W.m^{-1}.K^{-1}) is the thermal conductivity of ice equal to 2.2 W.m^{-1}.K^{-1}, ρ_w (kg.m^{-3}) the

748 water density, P_a (Pa) the air pressure, P_0 (Pa) a reference pressure equal to 1000hPa, and the

749 coefficients $k_1 = -0.06023$ W.m^{-1}.K^{-1}, $k_2 = 2.5425$ W.m^{-1} and $k_3 = 289.99$ K.

750 **APPENDIX B**

751 <u>*Wind-induced densification of near surface snow layers*</u>~~Compaction rate during snowdrift events~~

752 Following Brun et al. [1997], the compaction rate, ~~τ_{drift}~~τ_w, of <u>wind-induced densification of</u>

753 <u>near surface snow layers</u>~~the snow during snowdrift events~~ is computed using several steps. First, a

754 mobility index, Γ_{mob}, that describes the potential for snow erosion for each snow layer is computed

755 as a function of snow density:

756
$$\Gamma_{mob}(i) = a_{mob}\left[1.0 - \max\left(0, \frac{\rho_s(i) - \rho_{sn\min}}{\rho_{mob}}\right)\right] \tag{B1}$$

757 where $\rho_{snmin} = 50$kg.m^{-3} is the minimum density of snow, ρ_{mob} a reference density of 295kg.m^{-3},

758 and the dimensionless constant $a_{mob} = 1.25$. Secondly, a <u>wind-driven compaction</u>~~driftability~~ index,

759 ~~F_{drift}~~Γ_w, combining the mobility index and the near surface atmospheric wind speed:

760
$$\Gamma_w(i) = 1 - a_{\Gamma}\exp(-b_{\Gamma}\kappa_v V_a) + \Gamma_{mob}(i) \tag{B2}$$

761 where $\kappa_v = 1.25$ is a dimensionless coefficient for gust diagnosis from average wind speed, and the

762 constants $a_{\Gamma} = 2.868$ and $b_{\Gamma} = 0.085$ s.m^{-1}. A positive value of ~~F_{drift}~~ Γ_w indicates that <u>wind-driven</u>

763 compactionsnowdrifting can occur. Compaction rate from the surface is then propagated to the

764 layers beneath, following an exponential decrease, until it meets a snow layer having a negative

765 wind-driven compactiondriftability index. For each layer, this compaction rate is computed as

766 follows:

767 $\tau_w(i) = \dfrac{2\kappa_v \pi_\tau}{f_\tau(i)}$ with $f_\tau(i) = \max\left(0, \Gamma_w(i)\right) \times \exp\left(-a_\tau \sum\limits_{j=1}^{i} \left(\Delta z(j)(b_\tau - \Gamma_w(j))\right)\right)$ (B3)

768 where π_τ (s) is a time constant of one day, and the constants $a_\tau = 10$ and $b_\tau = 3.25$.

769 **APPENDIX C**

770 *Grid-cell snow fraction*

771 At regional and/or global scale the snow fraction, p_{sn}, for each patch of the ISBA land

772 surface model is computed as the sum between the bare ground snow covered fraction, p_{sng}, and

773 the fraction of vegetation covered by snow, p_{snv}, weighted by the vegetation fraction of the patches

774 covered by vegetation, f_{veg}. The snow fraction is thus computed as follows:

775 $p_{sn} = (1 - f_{veg})p_{sng} + f_{veg}p_{snv}$ $with$ $\begin{vmatrix} p_{sng} = \min\left(1, h_{sn}/h_{sng}\right) \\ p_{snv} = h_{sn}/\left(h_{sn} + w_{snv}z_{0veg}\right) \end{vmatrix}$ (C1)

776 where h_{sn} (m) is the total snow depth, h_{sng} (m) a ground snow depth threshold sets to 0.01m, z_{0veg}

777 (m) the vegetation roughness length, and w_{snv} a coefficient set to 2. f_{veg} is specified for each

778 vegetation patch. It is equal to 0.0 for bare soil, 0.95 for grassland/tundra as well as for temperate

779 and boreal forest, and varies exponentially according to the leaf area index (LAI) for crop types.

780 z_{0veg} varies for each vegetation type and is computed from typical vegetation height, h_{veg}, as

781 follows:

782 $z_{0veg} = \max\left(0.001, 0.13 \times h_{veg}\right)$ (C2)

783 For woody vegetation, h_{veg} is assumed constant over time. It ranges from 30m for tropical forests

784 and 20m for coniferous boreal forests to 15m, 10m or 5m for temperate forests and 2m for bushes.

785 For herbaceous plants, $h_{veg} = LAI/6$, with LAI the leaf area index given by the ECOCLIMAP

786   database. It ranges approximately from 0.01m to 0.8m for grassland/tundra. Finally, the height of

787   crop types is related to an exponential function of LAI and has a height of 1m before maturity

788   defined as a LAI of 3.5 $m^2.m^{-2}$. More details on these physiographic parameters can be found in

789   Masson et al. [2003].

REFERENCES

790

791   Adam, J. C., and D. P. Lettenmaier (2003), Adjustment of global gridded precipitation for

792   systematic bias, J. Geophys. Res., 108, 4257, doi:10.1029/2002JD002499, D9.

793   Anderson, E. A. (1976). A point energy and mass balance model of a snow cover. Silver Spring,

794   MD US. National Oceanic and Atmospheric Administration (NOAA). Technical Report NWS

795   19, 150 pp.

796   Armstrong, R. L., and E. Brun, Eds., 2008: Snow and Climate: Physical Processes, Surface

797   Energy Exchange and Modeling. Cambridge University Press, 222 pp.

798   Bartelt, P. and Lehning, M.: A physical SNOWPACK model for the Swiss avalanche warning:

799   Part I: numerical model, Cold Reg. Sci. Technol., 35, 123–145, 2002.

800   Beer, C., Fedorov, A. N., and Torgovkin, Y.: Permafrost temperature and active-layer thickness of

801   Yakutia with 0.5-degree spatial resolution for model evaluation, Earth Syst. Sci. Data, 5, 305-

802   310, doi:10.5194/essd-5-305-2013, 2013.

803   Beringer Jason, Amanda H. Lynch, F. Stuart Chapin III, Michelle Mack, and Gordon B. Bonan,

804   2001: The Representation of Arctic Soils in the Land Surface Model: The Importance of

805   Mosses. J. Climate, 14, 3324–3335. doi: http://dx.doi.org/10.1175/1520-

806   0442(2001)014<3324:TROASI>2.0.CO;2

807   Berrisford, P., Kållberg, P., Kobayashi, S., Dee, D., Uppala, S., Simmons, A. J., Poli, P. and Sato,

808   H. (2011), Atmospheric conservation properties in ERA-Interim. Q.J.R. Meteorol. Soc., 137:

809   1381–1399. doi:10.1002/qj.864

810   Best, M. J., Pryor, M., Clark, D. B., Rooney, G. G., Essery, R. L. H., M´enard, C. B., Edwards, J.

811   M., Hendry, M. A., Porson, A., Gedney, N., Mercado, L. M., Sitch, S., Blyth, E., Boucher, O.,

812   Cox, P. M., Grimmond, C. S. B., and Harding, R. J.: The Joint UK Land Environment

813   Simulator (JULES), Model description – Part 1: Energy and water fluxes, Geosci. Model Dev.,

814   4, 677–699, doi:10.5194/gmd-4-677-2011, 2011.

815   Boelter D. H.: Physical Properties of Peats as Related to Degree of Decomposition, Soil Science

816   Society of America Journal, Vol. 33 No. 4, p. 606-609, 1969,

817   doi:10.2136/sssaj1969.03615995003300040033x

818   Bohren, C. F., and B. R. Barkstrom (1974), Theory of the optical properties of snow, J. Geophys.

819   Res., 79(30), 4527–4535, doi:10.1029/JC079i030p04527.

820   Bonan GB, Shugart HH (1989) Environmental-factors and ecological processes in boreal forests.

821   Annu Rev Ecol Syst 20:1–28

822   Boone, A., and P. Etchevers, 2001: An intercomparison of three snow schemes of varying

823   complexity coupled to the same land-surface model: Local scale evaluation at an Alpine site. J.

824   Hydrometeor., 2, 374–394.

825   Boone, A., V. Masson, T. Meyers, and J. Noilhan, 2000: The influence of the inclusion of soil

826   freezing on simulations by a soil–vegetation–atmosphere transfer scheme. J. Appl. Meteor., 39,

827   1544–1569.

828   Braud, I., N. Varado, and A. Olioso (2005), Comparison of root water uptake modules using either

829   the surface energy balance or potential transpiration, Journal of Hydrology, 301, 267-286.

830   Brooks, R. H. and Corey, A. T.: Properties of porous media affecting fluid flow, Journal of the

831   Irrigation and Drainage Division, Vol. 92, No. 2, pp. 61-90, 1966.

832   Brown J., Hinkel K.M., & Nelson F.E. 2000. The Circumpolar Active Layer Monitoring (CALM)

833   program: historical perspectives and initial results. Polar Geography 24(3): 165-258.

834   Brown, J., O. Ferrians, J. A. Heginbottom, and E. Melnikov. 2002. Circum-Arctic Map of

835   Permafrost and Ground-Ice Conditions, Version 2. Boulder, Colorado USA. NSIDC: National

836   Snow and Ice Data Center.

837   Brown, R., Bartlett, P., MacKay, M., and Verseghy, D.: Evaluation of snow cover in CLASS for

838   SnowMIP, Atmos.-Ocean, 44, 223–238, doi:10.3137/ao.440302, 2006.

839   Brun, E., E. Martin, V. Simon, C. Gendre, and C. Cole´ou, 1989: An energy and mass model of

840   snow cover suitable for operational avalanche forecasting. J. Glaciol., 35, 333–342.

841   Brun, E., P. David, M. Sudul, and G. Brunot, 1992: A numerical model to simulate snow-cover

842   stratigraphy for operational avalanche forecasting. J. Glaciol., 38, 13–22.

843   Brun, E., E. Martin, and V. Spiridonov, 1997: Coupling a multi-layered snow model with a GCM.

844   Ann. Glaciol., 25, 66–72.

845   Brun Eric, Vincent Vionnet, Aaron Boone, Bertrand Decharme, Yannick Peings, Rémi Valette,

846   Fatima Karbou, and Samuel Morin, 2013: Simulation of Northern Eurasian Local Snow Depth,

847   Mass, and Density Using a Detailed Snowpack Model and Meteorological Reanalyses. J.

848   Hydrometeor, 14, 203–219. doi: http://dx.doi.org/10.1175/JHM-D-12-012.1

849   Campbell, G. S. (1974), A simple method for determining unsaturated conductivity from moisture

850   retention data, Soil Sci., 117, 311-314.

851   Canadell, J., R. B. Jackson, J. R. Ehleringer, H. A. Mooney, O. E. Sala, and E.-D. Schulze (1996)

852   Maximum rooting depth of vegetation types at the global scale. Oecologia, 108, 583–595.

853   Canal, N., Calvet, J.-C., Decharme B., Carrer, D., Lafont, S., and Pigeon, G. : Evaluation of root

854   water uptake in the ISBA-A-gs land surface model using agricultural yield statistics over

855   France, Hydrol. Earth Syst. Sci., 18, 4979-4999, doi:10.5194/hess-18-4979-2014, 2014.

856   Carmagnola, C. M., Morin, S., Lafaysse, M., Domine, F., Lesaffre, B., Lejeune, Y., Picard, G., and

857   Arnaud, L.: Implementation and evaluation of prognostic representations of the optical diameter

858   of snow in the SURFEX/ISBA-Crocus detailed snowpack model, The Cryosphere, 8, 417-437,

859   doi:10.5194/tc-8-417-2014, 2014.

860   Dankers, R., Burke, E. J., and Price, J.: Simulation of permafrost and seasonal thaw depth in the

861   JULES land surface scheme, The Cryosphere, 5, 773-790, doi:10.5194/tc-5-773-2011, 2011.

862   Decharme B. and H. Douville, 2006a: Uncertainties in the GSWP-2 precipitation forcing and their

863   impacts on regional and global hydrological simulations. Climate Dyn., 27, 695-713, DOI:

864   10.1007/s00382-006-0160-6

865   Decharme B. and H. Douville, 2006b: Introduction of a sub-grid hydrology in the ISBA land

866   surface model. Climate Dyn., 26, 65 - 78.

867 Decharme, B., H. Douville, 2007: Global validation of the ISBA Sub-Grid Hydrology. Climate

868   Dyn., 29, 21-37, doi:10.1007/s00382-006-0216-7

869 Decharme, B., A. Boone, C. Delire, and J. Noilhan (2011), Local evaluation of the Interaction

870   between Soil Biosphere Atmosphere soil multilayer diffusion scheme using four pedotransfer

871   functions, J. Geophys. Res., 116, D20126, doi:10.1029/2011JD016002.

872 Decharme, B., E. Martin, and S. Faroux (2013), Reconciling soil thermal and hydrological lower

873   boundary conditions in land surface models, J. Geophys. Res. Atmos., 118, 7819–7834,

874   doi:10.1002/jgrd.50631.

875 Dee, D. P., Uppala, S. M., Simmons, A. J., Berrisford, P., Poli, P., Kobayashi, S., Andrae, U.,

876   Balmaseda, M. A., Balsamo, G., Bauer, P., Bechtold, P., Beljaars, A. C. M., van de Berg, L.,

877   Bidlot, J., Bormann, N., Delsol, C., Dragani, R., Fuentes, M., Geer, A. J., Haimberger, L.,

878   Healy, S. B., Hersbach, H., Hólm, E. V., Isaksen, L., Kållberg, P., Köhler, M., Matricardi, M.,

879   McNally, A. P., Monge-Sanz, B. M., Morcrette, J.-J., Park, B.-K., Peubey, C., de Rosnay, P.,

880   Tavolato, C., Thépaut, J.-N. and Vitart, F. (2011), The ERA-Interim reanalysis: configuration

881   and performance of the data assimilation system. Q.J.R. Meteorol. Soc., 137: 553–597.

882   doi:10.1002/qj.828

883 Douville, H., Royer, J., and Mahfouf, J.: A new snow parameterization for the Meteo-France

884   climate model, Clim. Dynam., 12, 21–35, 1995.

885 Dutra, E., Balsamo, G., Viterbo, P., Miranda, P., Beljaars, A., Schär, C., and Elder, K.: An

886   improved snow scheme for the ECMWF land surface model: description and offline validation,

887   J. Hydrometeorol., 11, 899–916, 2010.

888 FAO/IIASA/ISRIC/ISSCAS/JRC, 2012. Harmonized World Soil Database (version 1.2). FAO,

889   Rome, Italy and IIASA, Laxenburg, Austria.

890 Farouki, O.T., (1986), Thermal Properties of Soils, Series on Rock and Soil Mechanics, 11, Trans

891   Tech Pub.,Rockport, MA, United States,136 pp Faroux S., A. T. Kaptué Tchuenté, J.-L.

892   Roujean, V. Masson, E. Martin, and P. Le Moigne (2013) ECOCLIMAP-II/Europe: a twofold

893 database of ecosystems and surface parameters at 1-km resolution based on satellite

894 information for use in land surface, meteorological and climate models. Geosci. Model Dev., 6,

895 563-582, doi:10.5194/gmd-6-563-2013.

896 Feddes, R.A., and Coauthors (2001), Modeling Root Water Uptake in Hydrological and Climate

897 Models, Bull. Amer. Meteor. Soc., 82(12), 2797-2809.

898 Fuchs, M., G. S. Campbell, and R. I. Papendick, An analysis of sensible and latent heat flow in a

899 partially frozen unsaturated soil, Soil Sci. Soc. Am. J., 42(3), 379-385, 1978.

900 Gouttevin, I., Krinner, G., Ciais, P., Polcher, J., and Legout, C.: Multi-scale validation of a new

901 soil freezing scheme for a land-surface model with physically-based hydrology, The

902 Cryosphere, 6, 407-430, doi:10.5194/tc-6-407-2012, 2012.

903 Joetzjer, E., Delire, C., Douville, H., Ciais, P., Decharme, B., Carrer, D., Verbeeck, H., De Weirdt,

904 M., and Bonal, D.: Improving the ISBACC land surface model simulation of water and carbon

905 fluxes and stocks over the Amazon forest, Geosci. Model Dev., 8, 1709-1727,

906 doi:10.5194/gmd-8-1709-2015, 2015.

907 Jordan, R.: A One-Dimensional Temperature Model for a Snow Cover: Technical Documentation

908 for SNTHERM. 89., Tech. rep., Cold Regions Research and Engineering Lab. Hanover NH,

909 1991.

910 Kuipers Munneke, P., van den Broeke, M., Lenaerts, J., Flanner, M., Gardner, A., and van de

911 Berg, W.: A new albedo parameterization for use in climate models over the Antarctic ice

912 sheet, J. Geophys. Res, 116, doi:10.1029/2010JD015113, 2011.

913 Lafaysse, M., S. Morin, C. Coléou, M. Vernay, D. Serça, F. Besson, J.-M. Willemet, G. Giraud

914 and Y. Durand, Towards a new chain of models for avalanche hazard forecasting in French

915 mountain ranges, including low altitude mountains, Proceedings of the International Snow

916 Science Workshop Grenoble - Chamonix Mont-Blanc - 2013, 7-11 October, Grenoble, France,

917 162-166, 2013.

918   Lawrence, D. and Slater, A.: Incorporating organic soil into a global climate model, Clim.

919   Dynam., 30, 145–160, doi:10.1007/s00382-007-0278, 2008.

920   Lawrence, D. M., A. G. Slater, V. E. Romanovsky, and D. J. Nicolsky, (2008) The sensitivity of a

921   model projection of near-surface permafrost degradation to soil column depth and inclusion of

922   soil organic mater. J. Geophys. Res., 113, F02011, doi:10.1029/2007JF000883.

923   Letts MG, Roulet NT, Comer NT, Skarupa MR, Verseghy DL (2000) Parametrization of peatland

924   hydraulic properties for the Canadian Land Surface Scheme. Atmos Ocean 38:141–160

925   Loth, B., and H.-F. Graf (1998), Modeling the snow cover in climate studies: 1. Long-term

926   integrations under different climatic conditions using a multilayered snow-cover model, J.

927   Geophys. Res., 103(D10), 11313–11327, doi:10.1029/97JD01411.

928   Loth, B., H.-F. Graf, and J. M. Oberhuber, 1993: Snow cover model for global climate

929   simulations. J. Geophys. Res., 98, 10 451–10 464.

930   Luo, L., Robock, A., Vinnikov, K., Schlosser, C., Slater, A., Boone, A., Etchevers, P., Habets, F.,

931   Noilhan, J., Braden, H., Cox, P., de Rosnay, P., Dickinson, R., Dai, Y., Duan, Q., Etchevers, P.,

932   Henderson-Sellers, A., Gedney, N., Gusev, Y., Habets, F., Kim, J., Kowalczyk, E., Mitchell,

933   K., Nasonova, O., Noilhan, J., Pitman, A., Schaake, J., Shmakin, A., Smirnova, T., Wetzel, P.,

934   Xue, Y., Yang, Z. and Zeng, Q.: Effects of frozen soil on soil temperature, spring infiltration,

935   and runoff: Results from the PILPS2 (d) experiment at Valdai, Russia, J. Hydrometeorol., 4,

936   334–351, doi:10.1175/1525-7541(2003)4<334:EOFSOS>2.0.CO;2,2003.

937   Lynch-Stieglitz, M., 1994: The development and validation of a simple snow model for the GISS

938   GCM. J. Climate, 7, 1842–1855.

939   Manabe, S., (1969), Climate and ocean circulation 1. The atmospheric circulation and the

940   hydrology of the earth's surface. Mon. Wea. Rev., 97, 739-805.

941   Masson, V., Le Moigne, P., Martin, E., Faroux, S., Alias, A., Alkama, R., Belamari, S., Barbu, A.,

942   Boone, A., Bouyssel, F., Brousseau, P., Brun, E., Calvet, J.-C., Carrer, D., Decharme, B.,

943   Delire, C., Donier, S., Essaouini, K., Gibelin, A.-L., Giordani, H., Habets, F., Jidane, M.,

944 Kerdraon, G., Kourzeneva, E., Lafaysse, M., Lafont, S., Lebeaupin Brossier, C., Lemonsu, A.,

945 Mahfouf, J.-F., Marguinaud, P., Mokhtari, M., Morin, S., Pigeon, G., Salgado, R., Seity, Y.,

946 Taillefer, F., Tanguy, G., Tulet, P., Vincendon, B., Vionnet, V., and Voldoire, A.: The

947 SURFEXv7.2 land and ocean surface platform for coupled or offline simulation of earth surface

948 variables and fluxes, Geosci. Model Dev., 6, 929-960, doi:10.5194/gmd-6-929-2013,

949 2013.~~Masson, V., and Coauthors (2012) The SURFEXv7.2 land and ocean surface platform for~~

950 ~~coupled or offline simulation of Earth surface variables and fluxes. Geosci. Model Dev.~~

951 ~~Discuss., 5, 3771-3851, 2012~~

952 Morin, S., Lejeune, Y., Lesaffre, B., Panel, J.-M., Poncet, D., David, P., and Sudul, M.: A 18-years

953 long (1993 - 2011) snow and meteorological dataset from a mid-altitude mountain site

954 (Col de Porte, France, 1325 m alt.) for driving and evaluating snowpack models, Earth Syst. Sci.

955 Data Discuss., 5, 29–45, doi:10.5194/essdd-5-29-2012, 2012.

956 Nicolsky DJ, Romanovsky VE, Alexeev VA, Lawrence DM (2007) Improved modeling of

957 permafrost dynamics in Alaska with CLM3. Geophys Res Lett 34. doi:10.1029/2007GL029525

958 Niu GY, Yang ZL (2006) Effects of frozen soil on snowmelt runoff and soil water storage at a

959 continental scale. J Hydrometeorol, 7:937–952

960 Noilhan, J., and P. Lacarrère (1995), GCM gridscale evaporation from mesoscale modeling. J.

961 Climate, 8, 206-223.

962 Oleson, K. W., Lawrence, D. M., Bonan, G. B., Flanner, M. G., Kluzek, E., Lawrence, P. J.,

963 Levis, S., Swenson, S. C., Thornton, P. E., Dai, A., Decker, M., Dickinson, R., Feddema,

964 J., Heald, C. L., Hoffman, F., Lamarque, J.-F., Mahowald, N., Niu, G.-Y., Qian, T.,

965 Randerson, J., Running, S., Sakaguchi, K., Slater, A., Stockli, R., Wang, A., Yang, Z.-

966 L., Zeng, X., Zeng, X.: Technical Description of version 4.0 of the Community Land Model

967 (CLM),   NCAR/TN-478+STR,   2010,   doi:10.5065/D6FB50WZ

968 (http://opensky.ucar.edu/islandora/object/technotes:493).

969 Pahaut, E.: La métamorphose des cristaux de neige (Snow crystal metamorphosis), Monographies

970   de la Météorologie Nationale, No. 96, Météo-France, Direction de la météorologie nationale,

971   France, 58pp., 1976..Paquin J.-P. and L. Sushama, On the Arctic near-surface permafrost and

972   climate sensitivities to soil and snow model formulations in climate models, Clim Dyn (2015)

973   44:203–228. DOI 10.1007/s00382-014-2185-6

974 Parrens, M; Calvet, JC; de Rosnay, P; **Decharme, B**, 2014, Benchmarking of L-band soil

975   microwave emission models, REMOTE SENSING OF ENVIRONMENT, 140, 407-419, doi:

976   10.1016/j.rse.2013.09.017

977 Peters-Lidard, C. D., E. Blackburn, X. Liang, and E. F. Wood (1998), The effect of soil thermal

978   conductivity parameterization on surface energy fluxes and temperatures. *J. Atmos. Sci., 55*,

979   1209– 1224.

980 Poutou, E., G. Krinner, C. Genthon, and N. de Noblet-Ducoudré, 2004: Role of soil freezing in

981   future boreal climate change. Climate Dyn., 23, 621–639, doi:10.1007/s00382-004-0459-0.

982 Schleef, S., Löwe, H., and Schneebeli, M.: Influence of stress, temperature and crystal morphology

983   on isothermal densification and specific surface area decrease of new snow, The Cryosphere, 8,

984   1825-1838, doi:10.5194/tc-8-1825-2014, 2014.

985 Shrestha, M.,Wang, L., Koike, T., Xue, Y., and Hirabayashi, Y.: Improving the snow physics of

986   WEB-DHM and its point evaluation at the SnowMIP sites, Hydrol. Earth Syst. Sci., 14, 2577–

987   2594, doi:10.5194/hess-14-2577-2010, 2010.

988 Slater A. G., C. A. Schlosser, C. E. Desborough, A. J. Pitman, A. Henderson-Sellers, A. Robock,

989   K. Ya Vinnikov, J. Entin, K. Mitchell, F. Chen, A. Boone, P. Etchevers, F. Habets, J. Noilhan,

990   H. Braden, P. M. Cox, P. de Rosnay, R. E. Dickinson, Z-L. Yang, Y-J. Dai, Q. Zeng, Q. Duan,

991   V. Koren, S. Schaake, N. Gedney, Ye M. Gusev, O. N. Nasonova, J. Kim, E. A. Kowalczyk, A.

992   B. Shmakin, T. G. Smirnova, D. Verseghy, P. Wetzel, and Y. Xue, 2001: The Representation of

993   Snow in Land Surface Schemes: Results from PILPS 2(d). J. Hydrometeor, 2, 7–25. doi:

994   http://dx.doi.org/10.1175/1525-7541(2001)002<0007:TROSIL>2.0.CO;2

995   Sun, S., J. Jin, and Y. Xue, 1999: A simple snow–atmosphere–soil transfer (SAST) model. J.
996   Geophys. Res., 104, 19 587–19 579.

997   Szczypta, C., Decharme, B., Carrer, D., Calvet, J.-C., Lafont, S., Somot, S., Faroux, S., and
998   Martin, E.: Impact of precipitation and land biophysical variables on the simulated discharge of
999   European and Mediterranean rivers, Hydrol. Earth Syst. Sci., 16, 3351-3370, doi:10.5194/hess-
1000   16-3351-2012, 2012.

1001 Vergnes, J.-P., B. Decharme, and F. Habets (2014), Introduction of groundwater capillary rises
1002   using subgrid spatial variability of topography into the ISBA land surface model, J. Geophys.
1003   Res. Atmos., 119, doi:10.1002/2014JD021573.

1004 Vernay, M., M. Lafaysse, L. Mérindol, G. Giraud and S. Morin, Ensemble forecasting of
1005   snowpack conditions and avalanche hazard, Cold Reg. Sci. Technol.,
1006   doi:10.1016/j.coldregions.2015.04.010, In press .

1007 Verseghy, D. L., 1991: CLASS—a Canadian land surface scheme for GCMs. I: Soil model. Int. J.
1008   Climatol., 11, 111–133.

1009 Vionnet, V., Brun, E., Morin, S., Boone, A., Faroux, S., Le Moigne, P., Martin, E., and Willemet,
1010   J.-M.: The detailed snowpack scheme Crocus and its implementation in SURFEX v7.2, Geosci.
1011   Model Dev., 5, 773-791, doi:10.5194/gmd-5-773-2012, 2012.

1012 Walter KM, Zimov SA, Chanton JP, Verbyla D, Chapin FS (2006) Methane bubbling from
1013   Siberian thaw lakes as a positive feedback to climate warming. Nature 443:71

1014 Wang, W., Rinke, A., Moore, J. C., Cui, X., Ji, D., Li, Q., Zhang, N., Wang, C., Zhang, S.,
1015   Lawrence, D. M., McGuire, A. D., Zhang, W., Delire, C., Koven, C., Saito, K., MacDougall,
1016   A., Burke, E., and Decharme, B.: Diagnostic and model dependent uncertainty of simulated
1017   Tibetan permafrost area, The Cryosphere, 10, 287-306, doi:10.5194/tc-10-287-2016, 2016.W.
1018   Wang, A. Rinke, J. C. Moore, X. Cui, D. Ji, Q. Li, N. Zhang, C. Wang, S. Zhang, D. M.
1019   Lawrence, A. D. McGuire, W. Zhang, C. Delire, C. Koven, K. Saito, A. MacDougall, E. Burke,

1020   ~~and B. Decharme: Diagnostic and model dependent uncertainty of simulated Tibetan~~

1021   ~~permafrost area, The Cryosphere Discuss., 9, 1769-1810, 2015~~

1022   Warren, S.: Optical properties of snow, Rev. Geophys. Space Phys., 20, 67–89, 1982.

1023   Yen, Y. C.: Review of thermal properties of snow, ice and sea ice, Tech. Rep. 81–10, Cold Reg.

1024   Res. and Eng. Lab., Hanover, NH, USA, , 1981.

1025   Zeng, X., Y.-J. Dai, R.E. Dickinson, and M. Shaikh, (1998), The role of root distribution for land

1026   climate simulation. Geophys. Res. Lett., 25, 4533-4536.

1027   Zhang T, Barry R, Gilichinsky D (2001) Russian historical soil temperature data. Digital media.

1028   National Snow and Ice Data Center, Boulder

1029   Zimov SA, Schuur EAG, Chapin FS (2006) Permafrost and the global carbon budget. Science

1030   312:1612–1613

1031

1032 **Table 1** – The peat soil hydraulic and thermal parameter values used in ISBA for fibric and sapric

1033 soil. w_{sat} (m^3.m^{-3}) is the prorosity, w_{fc} (m^3.m^{-3}) the water content at field capacity specified as

1034 matric potential at -0.1 bar for peat soil, w_{wilt} (m^3.m^{-3}) the water content at wilting point (matric

1035 potential of -15 bar), b the dimensionless shape parameter of the soil-water retention curve, ψ_{sat}

1036 (m) the soil matric potential, k_{sat} (m.s^{-1}) the soil hydraulic conductivity at saturation, c (J.m^{-3}.K^{-1})

1037 the soil heat capacity of organic matter, λ_s (W.m^{-1}.K^{-1}) the thermal conductivity of soil matrix, and

1038 λ_{dry} (W.m^{-1}.K^{-1}) the dry soil thermal conductivity. For pedotransfer functions of Boelter [1969], the

1039 fiber content in fibric soil is assumed to be equal to 76.8 % against 21.8 % in sapric soil in order to

1040 reach soil porosity values close to Letts et al. [2000]. The method for averaging mineral soil

1041 properties with peat soil values using the fraction of soil that is organic is also given for each

1042 parameter.

α_{peat}	Fibric soil	Sapric soil	Sources	Mineral/Peat average
w_{sat}	0.930	0.845	Letts et al. [2000] and Boelter [1969]	Arithmetic
w_{fc}	0.369	0.719	PTF from Boelter [1969]	Arithmetic
w_{wilt}	0.073	0.222	PTF from Boelter [1969]	Arithmetic
b	2.7	12	Letts et al. [2000]	Arithmetic
ψ_{sat}	-0.0103	-0.0101	Letts et al. [2000]	Arithmetic
k_{sat}	$2.8\ 10^{-4}$	$1.0\ 10^{-7}$	Letts et al. [2000]	Geometric
c	$2.5\ 10^{-6}$	$2.5\ 10^{-6}$	Farouki [1986]	Arithmetic
λ_s	0.25	0.25	Farouki [1986]	Geometric
λ_{dry}	0.05	0.05	Farouki [1986]	Geometric

1043

1043 **Table 2** – Daily skill scores simulated by each experiment at Col de Porte for snow depth, SWE,

1044 albedo and soil temperature at 10cm over the number of point measurement, *n*. The bias, centred

1045 root mean square errors (c-rmse) and square correlation (r^2) described in section 4.1 are shown.

1046 The best scores are given in bold.

	Period	Criterion	Experiments			
			CTL	SNL	CPT	NEW
Snow depth (m)	DJF (n=1624)	bias	0.126	0.108	**0.074**	0.089
		c-rmse	0.159	0.157	**0.126**	0.130
		r^2	0.863	0.870	**0.907**	0.900
	MAM (n=1656)	bias	0.165	0.127	0.077	**0.027**
		c-rmse	0.223	0.192	0.169	**0.155**
		r^2	0.845	0.878	0.884	**0.900**
	All (n=4737)	bias	0.102	0.082	0.053	**0.041**
		c-rmse	0.176	0.157	0.130	**0.126**
		r^2	0.889	0.908	0.923	**0.927**
SWE (kg.m^{-2})	DJF (n=835)	bias	12.329	6.196	**4.934**	8.887
		c-rmse	38.331	35.004	**34.476**	36.079
		r^2	0.901	0.913	**0.915**	0.911
	MAM (n=887)	bias	25.022	19.064	16.352	**0.334**
		c-rmse	61.138	57.204	55.699	**49.583**
		r^2	0.861	0.872	0.876	**0.900**
	All (n=2310)	bias	13.851	9.169	7.648	**2.981**
		c-rmse	45.641	42.267	41.134	**38.100**
		r^2	0.902	0.910	0.913	**0.924**
Albedo (-)	DJF (n=1456)	bias	0.047	0.047	0.047	**0.045**
		c-rmse	0.076	0.076	0.076	**0.074**
		r^2	0.528	**0.535**	0.533	0.506
	MAM (n=1516)	bias	0.077	0.077	0.076	**0.023**
		c-rmse	0.119	0.117	0.115	**0.080**
		r^2	0.768	0.785	0.792	**0.889**
	All (n=4101)	bias	0.048	0.046	0.045	**0.026**
		c-rmse	0.101	0.098	0.098	**0.082**
		r^2	0.858	0.869	0.871	**0.905**
Soil temperature 10cm (K)	DJF (n=1323)	bias	-1.082	-1.009	**-0.962**	-1.032
		c-rmse	0.892	0.837	**0.797**	0.811
		r^2	0.234	0.234	0.272	**0.279**
	MAM (n=838)	bias	-0.646	-0.624	-0.606	**-0.199**
		c-rmse	2.109	1.995	1.967	**1.701**
		r^2	0.827	0.848	0.852	**0.896**
	All (n=2237)	bias	-1.121	-1.079	-1.049	**-0.936**
		c-rmse	1.650	1.591	1.569	**1.519**
		r^2	0.871	0.880	0.883	**0.894**

1047

FIGURE CAPTIONS

1048 **Figure 1 –** Spatial distribution of the observed soil organic carbon content over two soil horizon

1049 (0-30cm and 30-70cm) at 0.5° by 0.5° resolution. Observations come from the Harmonized World

1050 Soil Database at 1 km resolution of the Food and Agricultural Organization.

1051 **Figure 2 –** Parameterization of the effect of soil organic carbon (SOC) on soil hydraulic and

1052 thermal properties. The soil organic carbon density profile, ρ_{soc}, is given by Equation 21 using a

1053 top soil organic carbon content of 10 kg.m^{-2}, a sub soil content of 15 kg.m^{-2}, and via a simple

1054 linear interpolation at each soil grid nodes that conserves the total soil carbon mass. The fraction of

1055 the soil that is organic, f_{soc}, in each layer is determined assuming a simple relationship between this

1056 last soil organic carbon density profile and an idealized peat soil density profile (Equation 22).

1057 Examples for the soil porosity, w_{sat}, the soil saturated hydraulic conductivity, k_{sat}, and the soil heat

1058 capacity, c, are given. Dotted lines represent vertical homogeneous mineral soil properties, dashed

1059 lines the idealized peat soil properties, and plain lines the resulting combined soil properties using

1060 averaging method sums-up in Table 1.

1061 **Figure 3 –** Overview of the four experiments performed at the Col de Porte field site. Daily

1062 simulated and observed data for snow depth (top) and SWE (bottom) are provided for 18 and 10

1063 years respectively. In-situ observations are in black, the *CTL* simulation in blue, *SNL* in green,

1064 *CPT* in orange, and *NEW* in red. The corresponding statistics are given in terms of annual bias and

1065 c-rmse for each year by measurements periods.

1066 **Figure 4 –** As Figure 3 but for surface albedo (top) and soil temperature at 10 cm depth (bottom).

1067 **Figure 5 –** Daily mean annual cycles of snow depth, SWE, surface albedo, and soil temperature at

1068 10 cm depth simulated (colours) and observed (black) at the Col de Porte field site. The

1069 corresponding skill scores are given in Table 2. Over all panels, the grey shadow corresponds to

1070 the uncertainty in in-situ measurements as discussed in section 4.1. The observed snow depth

1071 exhibits an accuracy of ±1cm, the soil temperature is measured with a precision of ±1K, while

1072 uncertainties in SWE and surface albedo is near ±10%.

1073   **Figure 6** – Daily mean annual cycles of snow density (kg.m^{-3}) and snowpack internal temperature

1074   (°C) simulated by the four experiments over 18 years at the Col de Porte field site.

1075   **Figure 7** – Quantitative comparison between observed (plain circles) and simulated (plain fields)

1076   daily snow depth and monthly soil temperature at 20cm and 160cm depths over the Northern-

1077   Eurasia. Results from the bare soil sub-grid patch alone of the *NEW-SOC* simulation are presented

1078   because in-situ measurements have been collected in open areas following the WMO standards as

1079   mentioned in section 5.1.

1080   **Figure 8** – Mean annual cycles of observed and simulated daily snow depth and monthly soil

1081   temperature profiles. The mean cycles are computed by averaging all simulated or observed mean

1082   annual cycles at each station. However, ~~global~~total skill scores (bias and c-rmse) found in each

1083   panel are computed merging together all simulated or observed time series of all stations over the

1084   entire observed periods.

1085   **Figure 9** – Daily snow depth skill scores (bias and c-rmse) simulated by the *CTL* and the *NEW*

1086   experiments during winter (DJF) and spring (MAM) over the Northern-Eurasia and expressed in

1087   meters. ~~Global~~ Total scores given between parentheses are computed by merging together all

1088   simulated or observed daily time series of all stations for each season.

1089   **Figure 10** – Monthly soil temperature skill scores at 20cm and 160cm depths simulated by the

1090   *CTL* and the *NEW* experiments during winter and expressed in degrees Celsius. ~~Global~~ Total

1091   scores (bias and c-rmse) are given for each panel.

1092   **Figure 11** – Monthly soil temperature profile bias simulated by the *NEW* (left) and the *NEW-SOC*

1093   (right) experiments during summer and expressed in degrees Celsius. ~~Global~~ Total skill scores

1094   (bias; c-rmse) are given in the top-panel for each soil horizon.

1095   **Figure 12** – Distribution of permafrost characteristics. The NSIDC estimated limits of continuous,

1096   discontinuous, sporadic and isolated permafrost regions are shown in the top panel. In each panel

1097   the red lines correspond to the observed boundary of the entire permafrost region. In the middle

1098   and the bottom panels, the mean active layer thicknesses simulated over the 1990-2013 period by

1099   the *NEW* and the *NEW-SOC* experiments are shown and compared to observations from the

1100   CALM network (circles). Total skill scores are given for each experiment.~~The all year mean~~

1101   ~~maximum active layer thicknesses simulated by the *NEW* and the *NEW-SOC* experiments are~~

1102   ~~shown in the middle and the bottom panels respectively.~~

1103   **Figure 13 –** Estimated and simulated active layer thicknesses over the Yakutia region. Estimations

1104   before the 1990s are given by Beer et al. [2013] ~~and~~ while the *NEW* and the *NEW-SOC*

1105   experiments are ~~represented~~averaged over the 1979-1990 period. The estimated and simulated

1106   latitudinal zonal averages are shown over the last panel where Beer et al. [2013] estimations are in

1107   black, *NEW* in blue and *NEW-SOC* in red. Dashed lines correspond to uncertainties in active layer

1108   thicknesses estimations computed using standard deviations provided with the dataset.